Master's Dissertation

A CFD Framework for Aeroelastic Gust Load Calculations

Author:

William Liw Tat Man

Supervisor:

Prof. Arnaud Malan

A thesis submitted in candidature for the degree of Master of Science in Engineering

Department of Mechanical Engineering
Industrial Computation Fluid Dynamics Research Group

Feb 2018

The financial assistance of the National Research Foundation (NRF) towards this research is hereby acknowledged. Opinions expressed and conclusions arrived at, are those of the author and are not necessarily to be attributed to the NRF.

Plagiarism

I know the meaning of plagiarism and declare that all the work in the document, save for that which is properly acknowledged, is my own. This thesis/dissertation has been submitted to the Turnitin module (or equivalent similarity and originality checking software) and I confirm that my supervisor has seen my report and any concerns revealed by such have been resolved with my supervisor.

Signature: Signed by candidate

Date: 23/02/18

Abstract

A Computational Fluid Dynamics (CFD) framework for the simulation of the aeroelastic response of aircraft flying under gust loading was developed. The multiphysics, Finite Volume, Vertex-Centered code Elemental® was employed and calculations were performed for the transonic flow regime. In the structural domain, the fuselage was treated as rigid and the wing was considered for aeroelastic calculations. The latter was represented by a beam stick model using Timoshenko beam theory in Elemental®'s structural module. The case under consideration was the NASA Common Research Model (CRM) flying at Ma = 0.86 with a 30 ft gust applied over the aircraft. Key contributions of this work included implementation of a computationally efficient gust model as well as the development of a fluid-structure interface. The latter was to transfer forces from a deforming wing skin to the wing-beam in a conservative manner while reflecting the resulting displacements on the wing surface. An interface library was developed for this purpose and 3rd order accurate Bezier curves used to recover a smooth deformed wing. The various sub-components of the aeroelastic model were rigorously validated. Following this, the developed framework was applied to the CRM under gust load conditions.

"If I have seen further, it is by standing on the shoulders of giants."

(Isaac Newton)

Acknowledgements

My sincere gratitude goes to my thesis supervisor Prof. Arnaud Malan for his invaluable guidance and insight. Without him, this thesis would never have seen the light of day. The members of team *Galjoen Vissie* and the researchers of the InCFD group at large were also particularly helpful in matters of the Elemental® code and CFD in general.

The Department of Aerospace Engineering at the university of Bristol, a partner on the Aerogust project, shared a library of material and made this research possible. Moreover, they were always available for further information or clarifications. Special thanks go to Prof. Jonathan Cooper, Dr Chris Wales and Dr Robbie Cook.

Computations were performed on the InCFD node hosted at the Chimera facilites of the Chemical Engineering department. Graham Inggs of the department was very prompt to assist in any issues that arose and I would like thank him for his patience in dealing with me.

Finally, many thanks go to my friends and family who were here during my low moments and listened to my numerous rants. I apologise for all the pain I put you through.

Contents

List of Figures

List of Tables

Nomenclature

Greek Symbols

$\boldsymbol{\theta}$	Rotation vector
β	User defined parameter for Newmark method
Δ	Deflection
γ	Ratio of specific heat
κ	Shear correction factor
ν	Poisson ratio
ρ	Density
τ	Twist
ξ	User defined parameter for Newmark method

Mathematical Operator

δ	Kronecker delta operator

Roman Symbols

$\boldsymbol{u}$	Velocity vector
$\mathcal{A}$	Bounded Surface
$\mathcal{V}$	Computational Volume

ω	shape function
$\mathbf{B}$	Shape function derivative matrix
$\mathbf{C}$	Damping matrix
$\mathbf{F}$	Flux Vector
$\mathbf{f}_{aero}$	Aerodynamic force
$\mathbf{h}$	Height vector
$\mathbf{l}$	Beam element unit vector
$\mathbf{M}$	Mass matrix
$\mathbf{m}$	Displacement vector
$\mathbf{N}$	Shape function matrix
$\mathbf{n}$	Unit normal vector
$\mathbf{R}$	Residual matrix
$\mathbf{r}$	Displacement vector
$\mathbf{S}$	Vector of source term
$\mathbf{U}$	Vector of unknown conservative variable
$\mathbf{u}$	Trial solution
$\mathbf{v}$	Mesh velocity vector
E	Elastic modulus
A	Area
a	Distance from node 0 to projected point
A_s	Amplitude Scaling
b	Distance from node 1 to projected point

C_p	Coefficient of pressure
E	Energy
F_g	Alleviation factor
F_s	Internal shear force
G	Shear modulus
H	Gust gradient
I	Moment of intertia
J	Polar moment of area
K	Stiffness matrix
L	Element length
M	Moment
P	Applied force
p	Pressure
q	Distributed load
s	Distance penetrated by gust
T	Torque
u	Velocity
U_g	Gust design velocity
U_{ref}	Reference velocity
v	Moving reference frame velocity
w	Velocity relative to the moving reference frame
x_j	Coordinate position in the j-direction

Superscripts

j	j index

Subscript

g	Gust
i	i index

Chapter 1

Introduction

1.1 Background and Project Motivation

The aircraft industry is at a pivotal point in its development. The advent of new players in the market coming from China and Brazil puts increased pressure on the traditional players from America and Europe. At the same time, the industry faces a new set of challenges to produce leaner and cleaner aircraft as environmental concerns and the prospect of fuel scarcity looms ahead. In fact, the European Union (EU) has committed to drastically reduce the fuel consumption and decrease CO_2 emissions of commercial aircraft by 75% (compared to 2000 levels) by 2050 [1]. To reach such a target, the call has been made for innovative and improved models to better understand natural phenomena and faciliate the development of new aircraft models via a variety of programmes such as Horizon2020 (H2020) [2].

Increasingly, Computational Fluid Dynamics (CFD) and numerical simulations are becoming more prevalent in the engineering world and in particular in the aviation industry. The latter has always had an interest in the field since a few percent increase in fuel efficiency goes a long way for airlines. In fact, the continous decrease in the cost of computing [3] makes the development and use of increasingly complex models more attractive. While computational meshes in the 1990s were confined to 2D and a few thousand grid points [4, 5], nowadays 3D simulations with tens of millions of nodes are standard practice [6–8].

In aeronautic simulations, a frequent assumption taken is that the aircraft structure undergoes only geometrically linear deformations. Even this deformation can result in an uncontrolled vibration phenomena known as flutter and can lead to catastrophic failure [9]. Historically, flutter has been dealt with by stiffening the structure and through extensive testing to ensure that it does not occur under normal flight conditions. Moreover, computer models and simulations are increasingly being used to predict the onset of flutter and faciliate the design process.

In aeroelasticity, the study of gust related loads is becoming increasingly important as it possibly represents the next major hurdle to overcome. The H2020 Aerogust consortium was formed and comprises of leading partners in the aviation industry stemming from both private companies and universities. Its focus is on the investigation and development of improved gust methods to meet the Flightpath 2050 goals [10]. The consortium has chosen this focus since gust loads can potentially contribute to the maximum permissible loads of an aircraft in service.

Low-fidelity methods such as the Doublet-Lattice Method (DLM) and the Unsteady Vortex-Lattice Method (UVLM) are commonly employed in aircraft aeroelasticity analysis. In the UVLM, a series of horsehoe vortices is used to calculate the lift and drag while the wing is idealised as an infinitely thin surface. Similarly in the DLM, a set of acceleration potential doublets is used to calculate the lift or force coefficient [11]. In fact, the two methods are equivalent for a steady state case. Originally, the Vortex-Lattice Method (VLM) was developed for steady flow but was later extended for transient calculations [12]. The main advantage of these two methods over CFD is the reduced computational cost. However, Reimer et al. [13] have shown that a CFD-based approach performed better that a DLM-based approach in predicting gust load factors in both the subsonic and transonic regime . The aim of this study was therefore to build a high fidelity aeroelastic model to predict the gust response of an aircraft.

To develop such a high fidelity aeroelastic model, the inviscid unsteady Euler equation set presents an adequate trade-off between accuracy and cost of computation to describe the fluid flow in a continuum. Two classical kinematical descriptions are in use, namely the Lagrangian and the Eulerian reference frame [14]. In the Lagrangian reference frame, an individual node is pinned to a material point and the two move in unison. Therefore this methodology enables deformation to be easily tracked and is widely used in structural mechanics. However, large deformation will result in distortion of the mesh and the mesh quality will suffer if no remeshing occurs. In the Eulerian reference frame, a mesh node is fixed in space and the material flows through the mesh and this method is commonly used for fluid flow description. For the purpose of Fluid-Surface interaction (FSI) calculations, a blend of the two methods called Arbitary Lagrangian Eulerian (ALE) is commonly employed [15–17]. The latter combines both to describe problems involving the interaction between fluid flow and structural deformation.

There are two main approaches to introduce the gust in a CFD calculation: via a Farfield Boundary Condition (FBC) or using a prescribed velocity method. In FBCs, numerical dissipation occurs as the gust travels through the domain where the gust is typically orders larger than the aircraft being modelled. To avoid this, the mesh required would have to be much finer than would otherwise be required resulting in a dramatic increase in computational cost [18]. Alternatively, local refinement around the gust as it travels through the domain could be performed but a mesh generator would need to be coupled to the flow solver, creating much added complexity. A prescribed velocity method, which in effect injects the gust into the flow, would eliminate the need for either. The two main prescribed velocity methods are the Field Velocity Method (FVM) [18–21] and the Split Velocity Method (SVM) [18]. Both of these can be easily implemented into an ALE code due to a similar formulation although the SVM method contains additional source terms. These account for the effect of the aircraft on the propagating gust and Wales et al.[18] has shown that as a result, SVM offers more accurate results.

To describe the structure, only the wing is considered to be flexible in this work. The wing is a long slender body and can be represented as a cantilever beam attached to the fuselage [22–24]. Note that, it is a reasonable assumption to model the wing as an elastic body and the rest of the aircraft as rigid [22, 25]. Force and moment balances and the theory of elasticity are applied to represent the wing as a beam. To discretise the beam, a Finite Element Method (FEM) is the de facto method. Euler-Bernoulli beam theory, also known as classical beam theory is the most commonly used beam representation. However, a key assumption means that it neglects shear effects and to obtain a more accurate solution, the more general Timoshenko Beam Theory (TBT) may be required.

1.2 Overview and Purpose of Study

For this work, a framework for high fidelity transonic aeroelastic calculations of a full aircraft model under gust loading was developed. The FVM Vertex-Centered code Elemental® was used to calculate the aerodnamic loads by solving the inviscid unsteady Euler equation set. An ALE reference frame is employed to account for mesh movement and the SVM was followed to introduce the gust in the fluid. The wing structure is represented as a beam, for which the Elemental® Timoshenko beam module was utilised. A strongly coupled partitioned FSI method is used and as such, there is the need to communicate data (loads and displacements) between the wing surface and structural beam. An interface library was developed for this purpose. Kinematic conservation has to be respected and the work of McGuire et al. [26] is employed to transfer the forces from the fluid domain to the solid domain. The wing surface mesh is also to deform smoothly in sympathy to the structure. Third order Bezier curves are used to interpolate beam displacements in a smooth manner. The displacements are then transfered to the fluid mesh via radial basis functions.

Various test cases were used to verify and validate the code. As much as possible the cases chosen tested different parts of the code independently as well as incrementally ramping up the complexity. The final case analysed was a 3D NASA Common Research Model (CRM) in the transonic regime under gust loads, one of the gust cases selected for the H2020 Aerogust project. The results were then compared to those independently obtained by the University of Bristol. Note that due to the parallel mesh motion module in Elemental® not being complete, the CRM CFD was run with a rigid wing. The resulting aerodynamic force histories were then applied to the beam to compare computed deflections to that of the others.

1.3 Thesis Layout

The thesis is divided into 8 chapters and a short description of each chapter is given below.

- **Case Description**: The framework is intended for a full aircraft model and the geometry used, the NASA CRM, is described as well as the flow conditions employed.

- **Governing Equations and Solution Procedures**: The physics employed to describe the flow and the structure is given in the form of governing equations. Moreover, the spatial and temporal discretisations are formulated and key factors affecting the methodology discussed.

- **Mesh Generation**: In CFD simulations and in particular 3D cases, meshing is an integral part of the simulation and can be a time consuming exercise. Moreover, mesh quality can severely affect solution accuracy as well as simulation time [27]. This chapter describes the process of generating a suitable mesh for the CRM geometry.

- **Fluid Surface Interaction**: The theory used and the manner in which the interface library was developed is described.

- **Verification and Validation**: To build confidence in the code developed, verification and validation must be performed. The test cases employed are described and the results compared to analytical solutions where possible or to experimental results. The mesh refinement process for the CRM is also depicted.

- **Results**: The results of the final gust related simulation are presented and compared with the results obtained by the University of Bristol.

- **Conclusion and recommendations**: Conclusions are drawn from the performed studies and recommendations for improvements and future work are made.

Chapter 2

Case Description

In the late 2000s, various parties in the aerospace community expressed the desire for a new test case [28]. The need for a more modern geometry for CFD validation purposes was being felt. As such, the CRM geometry was proposed for the fourth Drag Prediction Workshop (DPW) in 2009 for drag and moment validation. Accordingly, the Aerogust consortium selected the CRM as a test case for aeroelastic calculations and it was also selected for this study. In this chapter, the geometric and structural descriptions of the CRM are given and the gust case of interest is defined.

2.1 Geometrical Description

The CRM's fuselage is representative of a wide body commercial transport aircraft designed with a transonic cruise speed of Mach number 0.85 and a nominal lift coefficient of 0.5. Different configurations were created including with and without tail and nacelle. These can be found on the website for the CRM [29]. For the purpose of this study, the wing/body/tail configuration was selected and can be seen in Fig 2.1. Table 2.1 gives the principle geometric characteristics while an extensive description can be found in the work by Vassberg et al. [28].

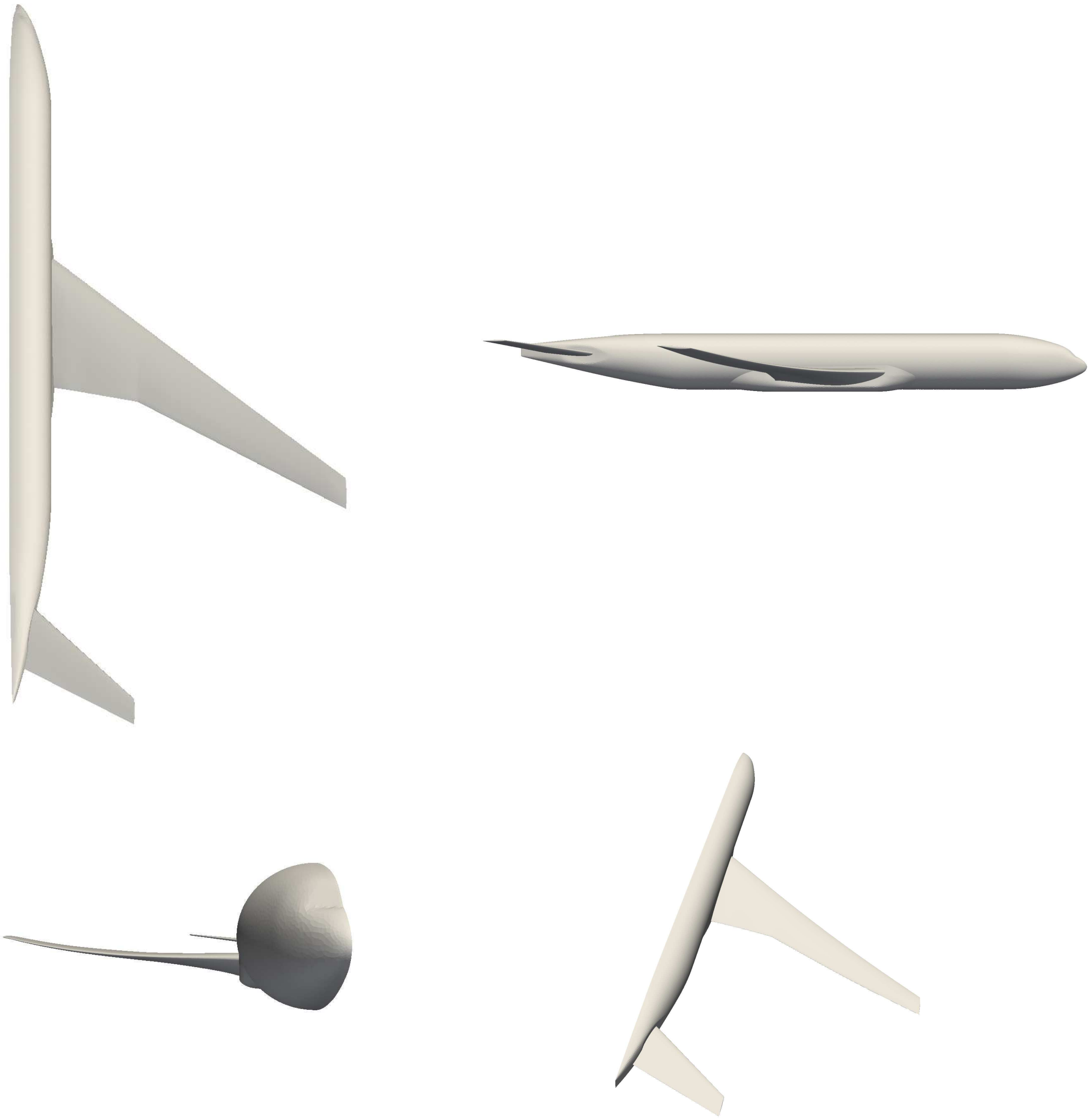

Figure 2.1 CRM Geometry

Table 2.1 *Main geometrical characteristic of the CRM*

Area (m^2)	383.7
Aspect Ratio	9
Reference chord length (m)	7.00
Span (m)	58.76

Table 2.2 *Modes for the CRM in MTOW configuration*

Mode	Frequency (Hz)
1	1.0574
2	1.4547

2.2 Structural Definition

A reduced order structural definition based on the FERMAT FEM model of Klimmek and further condensed by Cook et al. was used [30]. Using Patran®'s section tool, Cook reduced the FEM structure to a beam model by finding an equivalent neutral axis and the associated sectional properties [31]. The complexity of the system and the degrees of freedom are thus reduced and a simpler approach can be used to solve the system. Furthermore, previous studies have demonstrated that using a beam representation has a negligible effect on accuracy [23,32]. Cook also compared the modal frequencies between the beam representaion and the full FEM model and found the difference to be less than 10%.

Two mass configurations were derived by Klimmek namely a Maximum Take Off Weight (MTOW, 260 tons) and a Maximum Zero Fuel Weight (MZFW, 195 tons) [33]. The MTOW configuration with 100% fuel was used for the purpose of this work. Since the motion of the wing is dominated by the lowest frequency modes, only the first two mode shapes were used and they are given in Table 2.2 and illustrated in Fig 2.2 and Fig 2.3.

2.3 Aeroelastic and Gust Case

For the purpose of this work, an aeroelastic and transonic response of the CRM geometry under gust loading was of interest. To this effect, the flow conditions H suggested by Aerogust were employed and the values are summarised in Table 2.3. Moreover Aerogust advocates three different gust length to be investigated. Due to time restrictions, only the shortest gust length was investigated.

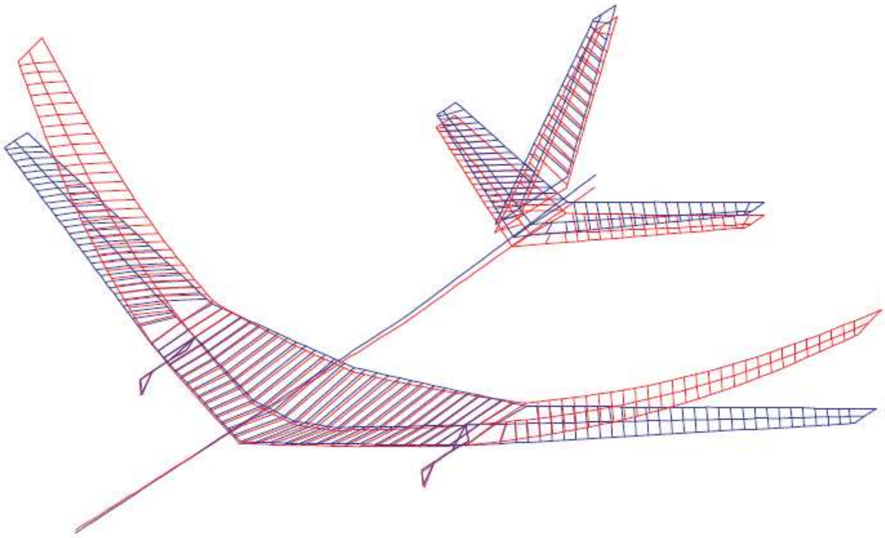

Figure 2.2 Mode 1 for MTOW configuration. Adapted from [34]

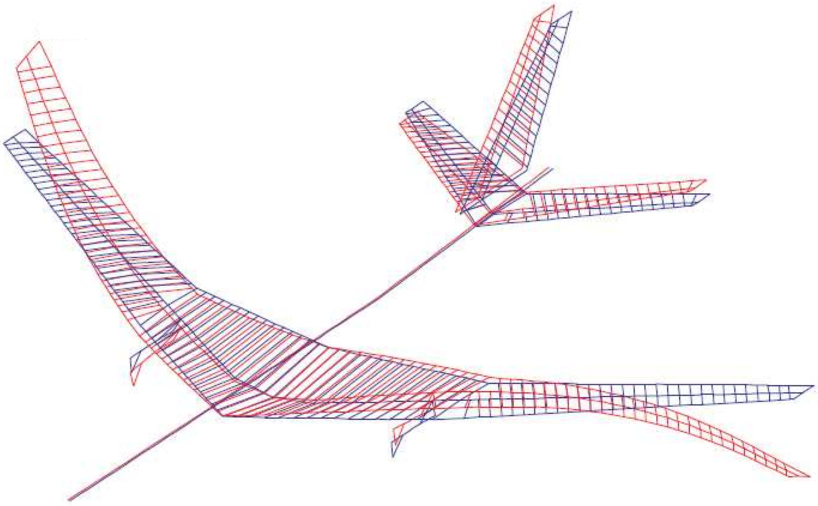

Figure 2.3 Mode 2 for MTOW configuration. Adapted from [34]

As per the Federal Aviation Regulations (FAR), the shape of the gust is given by

$$u_g = \frac{A_s U_g F_g}{2}\Big[1 - cos\Big(\frac{\pi s}{H}\Big)\Big] \tag{2.1}$$

with $0 \leq s \leq 2H$.

Table 2.3 *Flow definition for test case H obtained from [34]*

Flow condition	**H**
Mach number	0.86
Amplitude Scaling, A_s	0.781364
Alleviation factor, F_g	0.7785

Table 2.4 *Gust definition used obtained from [34]*

Half gust length (m)	9.144
Reference Velocity, U_{ref} (m/s)	17.07

Here, s and H are the distance penetrated by the gust and the gust gradient respectively. The alleviation factor, F_g, and the amplitude scaling, A_s, are given in Table 2.3 and the design gust velocity, U_g, in Equivalent Air Speed (EAS) is given by Eq (2.2)

$$U_g = U_{ref}\left(\frac{H}{106.68}\right)^{\frac{1}{6}} \tag{2.2}$$

where the nomenclature is as previously defined.

Chapter 3

Governing Equations and Solution Procedures

The aim of this project is to model the aeroelastic response of a 3D aircraft under gust loads. The inviscid unsteady Euler equation set is modified to include the ALE algorithm and the prescribed gust velocity SVM was employed. To describe the structural model, the fuselage was assumed to be rigid and only the wing was considered for aeroelastic purposes. Subsequently, a beam stick model using linear Timoshenko beam theory was employed. This chapter details the governing equations for the flow and the structure as well as the solution procedures.

3.1 Fluid Governing Equations

The governing equation set for the fluid domain is given by:

$$\frac{\partial \mathbf{U}}{\partial t} + \frac{\partial \mathbf{F}^j}{\partial x^j} + \mathbf{S}(\mathbf{U}) = 0 \tag{3.1}$$

with the terms being defined as:

$$\mathbf{U} = \begin{bmatrix} \rho\tilde{u}_i \\ \\ \rho \\ \\ \rho\widetilde{E} \end{bmatrix}, \mathbf{F}^j = \begin{bmatrix} w_j\rho\tilde{u}_i + p\delta_{ij} \\ \\ w_j\rho \\ \\ w_j\rho\widetilde{E} + p\tilde{u}_j \end{bmatrix}, \mathbf{S(U)} = \begin{bmatrix} s_m(u_{g,i}) \\ \\ 0 \\ \\ s_e(u_{g,j}) \end{bmatrix} \tag{3.2}$$

$$w_j = \tilde{u}_j + u_{g,j} - v_j \tag{3.3}$$

where x_j is a fixed Eulerian Cartesian reference frame axis j, w_j is the velocity relative to the moving reference frame and v_j is the moving mesh velocity. The fluid velocity, u_j, is split in two components as shown in Eq (3.4) resulting in a prescribed gust component, $u_{g,j}$, and a remainder velocity component denoted by the tilde overline.

$$u_j = u_{g,j} + \tilde{u}_j \tag{3.4}$$

U is the vector of variables to be solved and **F** is the vector of mass, momentum and energy flux. **S(U)** is the vector of source terms and its components are described in Eq (3.5) and Eq (3.6) [18].

$$s_m(u_{g,i}) = \rho\left[\frac{\partial u_{g,i}}{\partial t} + \sum_j^k (\tilde{u}_j + u_{g,j})\frac{\partial u_{g,i}}{\partial x^j}\right] \tag{3.5}$$

$$s_e(u_{g,j}) = \sum_j^k \left(\tilde{u}_j s_m(u_{g,j}) + p\frac{\partial u_{g,j}}{\partial x^j}\right) \tag{3.6}$$

The governing equation set, Eqn (3.1), can be cast in weak form by integrating over an arbitrary moving control volume $\mathcal{V}(t)$ bounded by a surface $\mathcal{A}(t)$.

$$\frac{\partial}{\partial t}\int_{\mathcal{V}(t)} \mathbf{U}d\mathcal{V} + \int_{\mathcal{A}(t)} \mathbf{F}^j n_j d\mathcal{A} + \int_{\mathcal{V}(t)} \mathbf{S}(\mathbf{U})d\mathcal{V} = 0 \tag{3.7}$$

where the nomenclature is as defined previously.

3.1.1 Fluid constitutive equations

To close the system of equations, the Ideal Gas Law was employed. It links pressure, temperature and density together and is independent of time. Temperature is not taken as a variable leaving three unknowns such that at any point in time the energy can be calculated if the other two are known.

$$E = \frac{p}{\rho(\gamma - 1)} + \frac{1}{2}\sum_{j}^{k} u_j^2 \tag{3.8}$$

where γ is the ratio of specific heat and is taken as 1.4. It should be noted that similar to the velocity, the total specific energy was also split into a prescribed gust component and a remainder component . However, the prescribed component, E_g, naturally drops out of the equations and $\widetilde{E}$ is defined by Eqn (3.9) [18].

$$\widetilde{E} = \frac{p}{\rho(\gamma - 1)} + \frac{1}{2}\sum_{j}^{k} \tilde{u}_j^2 \tag{3.9}$$

where the nomenclature is as defined previously.

3.1.2 Discretisation

As there is no general analytical solution to Equation (3.7), it has to be solved numerically and the equation has to be transformed from a continuous form to a discrete form. To that effect, a central difference or an upwind scheme could be employed. The latter is chosen as artificial dissipation is required in the former to avoid odd-even decoupling and smearing in the transonic regime [35]. Instead, a second order Monotonic Upwind for Conservation Law (MUSCL) scheme [36] with Van Albada limiter to eliminate spurious oscillations was employed. To identify the upwind direction, there are two major approaches; the Flux Vector Splitting (FVS) approach and the Godunov (also known as Riemann) approach. In turn, they give rise to the FVS and Flux Difference Splitting (FDS) family of schemes respectively [37]. In the FVS approach, the flux is split into a positive and negative term according to the sign of the eigenvectors and the schemes are generally simpler and more efficient than FDS schemes. However, this also leads to reduced accuracy compared to a Godunov type approach [37]. On the other hand, in an FDS scheme the flux is evaluated by solving Riemann's initial-value problem at the interface between two cells. In this work, the FDS scheme Harten-Lax-van Leer with Contact (HLLC) was utilised as Mowat showed that HLLC gives superior results to the Roe scheme and the Advection Upstream Splitting Method plus (AUSM+) for ALE calculations [15]. The basic HLLC-ALE code was available in Elemental® for this project. However, further work was required to implement the SVM method for gust modelling.

The temporal term was discretised using second order backward difference with a pseudo-time marching method. Furthermore, a four stage Runge-Kutta was then applied to improve computational efficiency. The equations and values of the coefficients are given by Lallemand [5]. To ensure stability, the size of the pseudo time step size was locally defined according to the largest eigenvalue and the effective mesh spacing [38].

3.1.3 Boundary condition

To close the system, appropriate boundary conditions have to be imposed. There is the need to bound the domain as it is unfeasible for it to extend indefinitely. Moreover, the interface between the skin of the aircraft and the fluid has to be defined. Futhermore, to reduce the cost of calculation the aircraft is assumed to be symmetrical and only half the aircraft with a symmetry plane is employed. For the farfield boundary, a Summation By Parts-Simultaneous Approximation Terms (SBP-SAT) far field boundary condition is employed [39].

A slip boundary was imposed on the symmetry plane as well as on the solid walls so that the fluid velocity normal to the boundary is equal to the moving boundary velocity.

$$\boldsymbol{u} \cdot \mathbf{n} = \mathbf{v} \cdot \mathbf{n} \tag{3.10}$$

where **u** is the velocity vector, **v** is the mesh velocity vector and **n** is the outward pointing normal to the boundary.

The slip boundary condition is weakly imposed by adding SAT to the right hand side of the governing equation [39]. Thus instead of the velocity being hard set, the variable is driven to the desired value during solving.

3.2 Solid Governing Equations

Timoshenko beam theory was used to describe the behaviour of the wing. Euler Bernoulli beam theory is another possible method and perhaps the one more commonly used [40]. However, Euler Bernoulli beam theory does not account for shear effects and assumes that the beam cross-section remains perpendicular to the beam axis during deformation [41]. Therefore Timoshenko beam theory was preferred to obtain greater accuracy. The properties of the beam were obtained from the H2020 Aerogust project partner, the University of Bristol.

3.2.1 Beam theory and kinematic assumptions

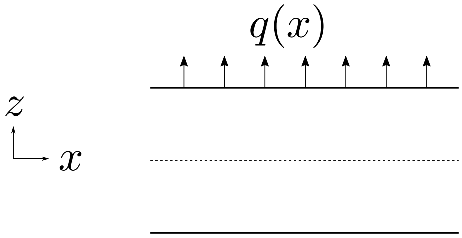

Figure 3.1 Schematic of a section of the beam

To derive the governing equations, a quasi-static beam running lengthwise in the x direction and with distributed force $q(x)$ applied as shown in Fig 3.1 was considered. An infinitesimal sliver of length dx of the beam was taken and a force and moment balance was performed (Fig 3.2). Originally, the thickness is assumed negligible such that only a planar element in the x-z plane need to be considered. The distributed force $q(x)$ acts on the element but since it is in equilibrium, the force must be balanced by internal shear forces and moments. A full derivation can be found in [23]. Simplifying and ignoring higher order terms give Equation (3.11) and(3.12).

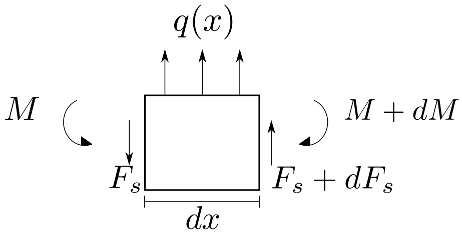

Figure 3.2 Resulting forces on an infinitesimal element of length dx due to a distributed load $q(x)$

$$\frac{dF_s}{dx} + q = 0 \tag{3.11}$$

$$\frac{dM}{dx} - F_s = 0 \tag{3.12}$$

where F_s is the internal shear force and M is the moment.

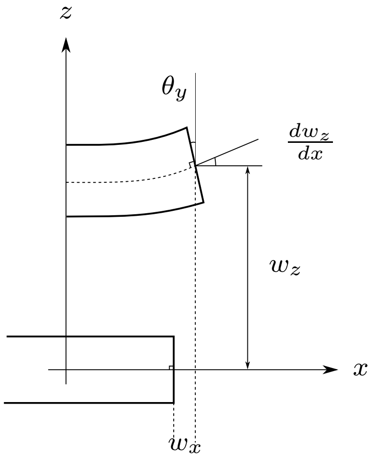

Figure 3.3 Diagram showing a beam section in its original and deformed position. Note that this is for the case where shear effect are neglected

As per beam theory, the beam cross-section (originally perpendicular to the x axis) remains planar and rigid thoroughout the deformation of the beam [41]. It then follows that the deformed position of the cross-section is fully defined by the displacement vector of its midpoint, $\mathbf{r}$, from its original position and a rotation vector $\boldsymbol{\theta}$. Another assumption applied was that the displacement would be small compared to the beam length such that $\sin\theta_i \approx \tan\theta_i \approx \theta_i$. These two assumptions constitute the basis for linear Timoshenko beam theory.

The displacement vector $\mathbf{m}$ of a point along the cross-section can then be derived. Applying the 2D simplification gives:

$$\mathbf{m} = \begin{bmatrix} m_x \\ m_y \\ m_z \end{bmatrix} = \begin{bmatrix} z\theta_y \\ 0 \\ r_z \end{bmatrix} \tag{3.13}$$

The definition of normal and shear stress and Hooke's law are applied to the force and moment balance to give the governing equations. A full derivation can be found in the work of Andersen and Nielsen [41].

$$\frac{\partial}{\partial x}\left[\kappa AG\left(\frac{\partial m_z(x,t)}{\partial x} - \theta_y\right)\right] + q(x,t) = 0 \tag{3.14}$$

$$\frac{\partial}{\partial x}\left(\mathrm{E}I\frac{\partial \theta_y}{\partial x}\right) + \kappa AG\left(\frac{\partial m_z(x,t)}{\partial x} - \theta_y\right) = 0 \tag{3.15}$$

where A is the area, E and G the elastic and shear modulus respectively, I the moment of inertia and κ is the shear correction factor. The strain is assumed constant over the cross-section but in reality, warping of the cross-section occurs and the shear correction factor is introduced to account for that effect.

Similarly, by taking a force balance in the axial direction and a torsional balance, the governing equation in the axial direction and for torsion respectively can be found.

3.2.2 Discretisation

For the spatial discretisation of the structure, a Finite Element Method (FEM) approach was employed with Newmark method for temporal discretisation. A smooth and arbitrary shape function ω is introduced to reduce the order of the governing equation from one second order differential to two first order differentials. A discussion about the degree of smoothness required to obtain a solution can be found in the work of Fish and Belytschko [40]. A formal proof of the equivalence between the weak and strong form is also provided. The next step is to approximate the function w, also known as a weight or trial function, using a shape function matrix $\mathbf{N}$. In what is known as the Galerkin FEM, the trial solution $\mathbf{u}$ is also approximated using the same shape function. The shape function derivative matrix $\mathbf{B}$ is also introduced. Moreover, the equation for each element can be gathered to obtain the global shape function matrix and its derivative.

$$\begin{aligned} \mathbf{u} &= \mathbf{N}\mathbf{U} \\ \omega &= \mathbf{N}\boldsymbol{\omega} \end{aligned} \tag{3.16}$$

$$\mathbf{B} = \frac{d\mathbf{N}}{dx} \tag{3.17}$$

Using the above-mentioned, the discretised governing equations can be obtained and the discrete axial equation is given by Equation (3.18).

$$\left[AE \int_{\Omega} \mathbf{B}^T \mathbf{B} dx\right] \mathbf{U} = \int_{\Omega} \mathbf{N}^T b dx + V \tag{3.18}$$

where V is the term due to the imposed boundary condition and $\mathbf{N}^T$ denotes the transpose of matrix $\mathbf{N}$. The rest of the nomenclature is as previously defined.

It can be seen that Eq (3.18) is in the form $\mathbf{KU} = \mathbf{R}$ with the coefficient of $\mathbf{U}$ on the LHS being the stiffness matrix $\mathbf{K}$ and $\mathbf{R}$ being the body forces (in this case axial forces) and imposed boundary condition. Furthermore, the relationship can be extended to include dynamic and viscous effects:

$$\mathbf{M}\ddot{\mathbf{U}} + \mathbf{C}\dot{\mathbf{U}} + \mathbf{K}\mathbf{U} = \mathbf{R} \tag{3.19}$$

where **M** and **C** are the mass and damping matrices respectively.

For the purpose of temporal discretisation, the Newmark method was used and the displacement, velocity and acceleration at the next time step are given by Equation (3.20) (3.21) (3.22) respectively [23].

$$\mathbf{U}^{t+\Delta t} = \mathbf{U}^t + \Delta t\dot{\mathbf{U}}^t + \Delta t^2\left[\left(\frac{1}{2} - \beta\right)\ddot{\mathbf{U}}^t + \beta\ddot{\mathbf{U}}^{t+\Delta t}\right] \tag{3.20}$$

$$\dot{\mathbf{U}}^{t+\Delta t} = \dot{\mathbf{U}}^t + \Delta t\left[(1 - \xi)\ddot{\mathbf{U}}^t + \xi\ddot{\mathbf{U}}^t\right] \tag{3.21}$$

$$\ddot{\mathbf{U}}^{t+\Delta t} = \frac{1}{\beta\Delta t^2}(U^{t+\Delta t} - U^t) - \frac{1}{\beta\Delta t}\dot{U}^t + \left(1 - \frac{1}{2\beta}\right)\ddot{U}^t \tag{3.22}$$

where ξ and β are user defined parameters and 1/2 and 1/4 are used to obtain an implicit and unconditionally stable method [42]. Furthermore, this choice of parameters yields a second order accurate method.

The above beam solving functionality was available in Elemental® at the start of this work. Further code development was then done to apply flow related forces to the beam solver and extract displacements such that the wing skin surface is deformed accordingly.

3.3 Parallel Computing

3D simulations require large domains with hundred of thousands if not millions of nodes. Additionally, the cost is further increased by the number of timesteps required for FSI calculations. Therefore, it would be computationally advantageous to decompose the fluid mesh into several domains to be solved by multiple cores concurrently. Since the iterative procedure employed is concerned only with neighbouring nodes, the calculation could be paralellised efficiently, with appropriate communication at the decomposed domain boundary. To that effect, the METIS library was used for the decomposition and the MPI library for the communication.

The beam representation is generally smaller than the fluid domain and in the order 10^2 [22, 24, 30]. Therefore, the cost of communication outways the benefit of solving the beam displacement on multiple parallel cores. The solid domain was thus set up to run on one core, with forces from all fluid mesh sub-domains being passed in and the updated wing position broadcasted to all fluid sub-domains.

3.4 Conclusion

In this chapter, the equations governing the fluid flow and the solid structure were described. The inviscid Euler equations set modified to contain a prescribed gust velocity component and moving mesh motion was employed for the flow. To that effect, SVM was implemented to introduce the gust in the domain. On the other hand, linear Timoshenko beam Theory was used to model the structure. Furthermore, the discretisation process was outlined. For the fluid, the MUSCL scheme was used for upwinding with a Van Albada limiter to eliminate spurious results and the HLLC scheme for the flux evaluation.. In the next chapter, the mesh generation process is described.

Chapter 4

Mesh Generation

Mesh quality is an important aspect of CFD simulations and can drastically affect solution accuracy and simulation time [27]. In general, the finer the mesh the better the accuracy as a finer mesh captures the physics better and reduces numerical dissipation. However, a finer mesh also increases the computational cost as there are more points to be resolved. Therefore it is important to find a good balance between accuracy and speed. The Pointwise® software was used for mesh generation using Delaunay triangulation.

As a starting point, the mesh spacing used by Changfoot for his mesh refinement study on the CRM was employed [39]. Specifically, his coarse mesh and his medium mesh was essentially blended together to improve efficiency. To keep the node count low, the nodes were concentrated around zones of interest with an aggressive growth strategy. For instance, the mesh spacing for the medium mesh at the wing tip was used and at the leading edge close to the wing tip. The edge length was then grown along the leading edge until the spacing close to the fuselage is the same as for the coarse mesh.

Table 4.1 *Table of the main values for the mesh used*

Max edge length on wing (mm)	225
Min edge length on wing (mm)	3.30
Total nodes (millions)	1.50

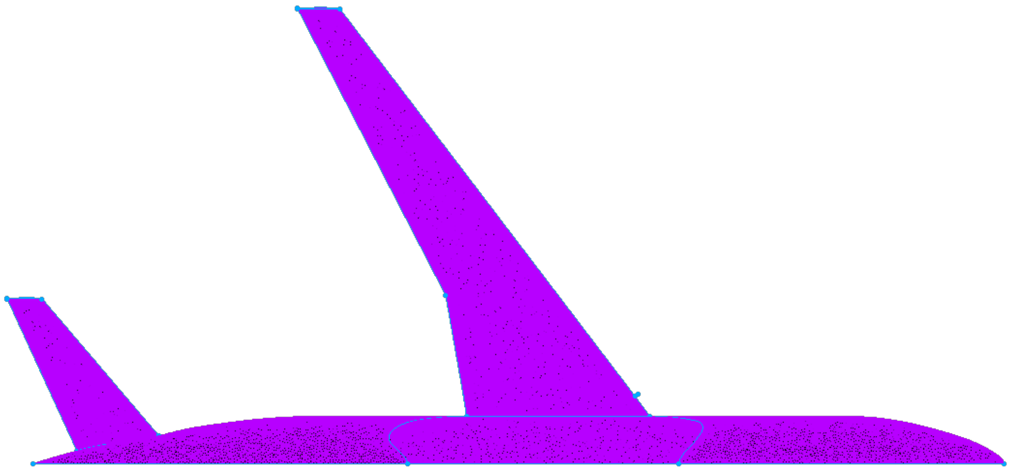

Figure 4.1 Surface mesh of the CRM

In addition, refinement blocks and baffles were used so as to constrain element growth in these regions and better capture the flow physics. In front of the leading edge, a zone of high pressure forms as the flow prepares to encounter an obstacle. To obtain a higher resolution in that region and to accelerate convergence, a refinement block was created in front of the leading edge (Fig 4.3 and 4.4). Similarly, a refinement baffle in the shape of a half tube was used around the wingtip (Fig 4.5).

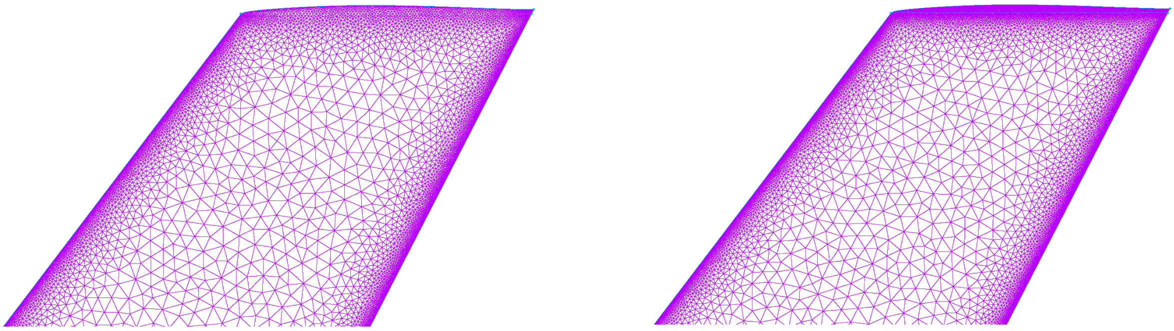

Figure 4.2 Surface mesh of the wing. On the left is Changfoot's coarse mesh and on the right is the refined mesh. It can be seen that the wing tip is more refined on the right.

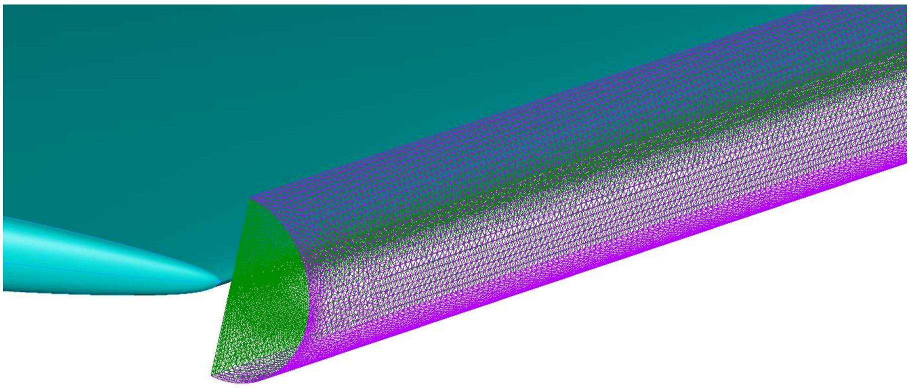

Figure 4.3 Refinement block in front of the leading edge

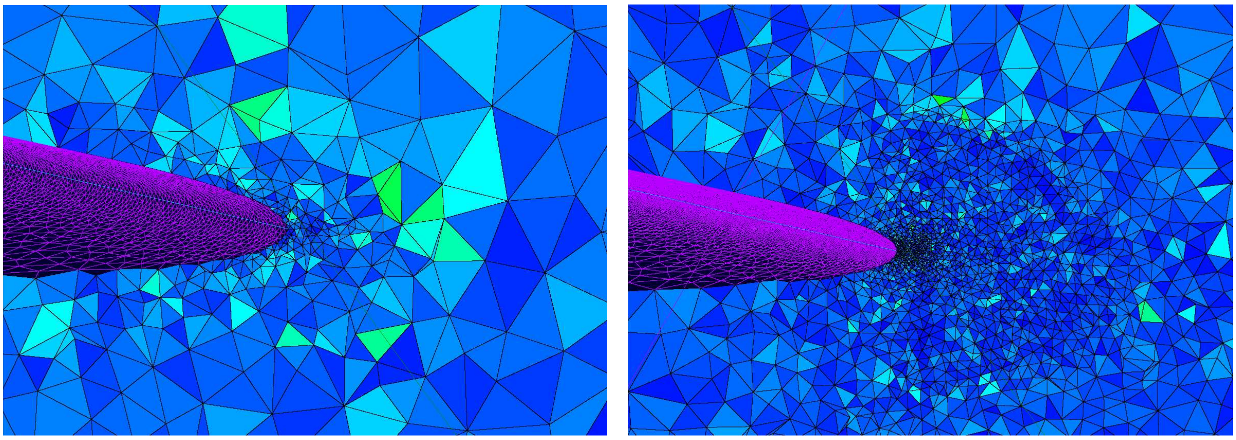

Figure 4.4 Cells around the leading edge. On the left is Changfoot's coarse mesh and on the right is the refined mesh. The effect of the refinement baffle can be seen on the right.

Moreover, the overall domain was separated into two regions with a smaller inner hemisphere and a coarser outer hemisphere to extend the domain. The inner region extends about 4.5 chord length in front and behind the aircraft, with the aircraft itself about 9 chord lengths. This region is constrained to a smaller edge length since the main flow gradients are prevalent in that region. The outer hemisphere has a diameter of 200 chord lengths centered about the aircraft. The overall mesh has 1.50M nodes with the majority of the nodes found in the inner region. Table 4.1 summarises key mesh parameters.

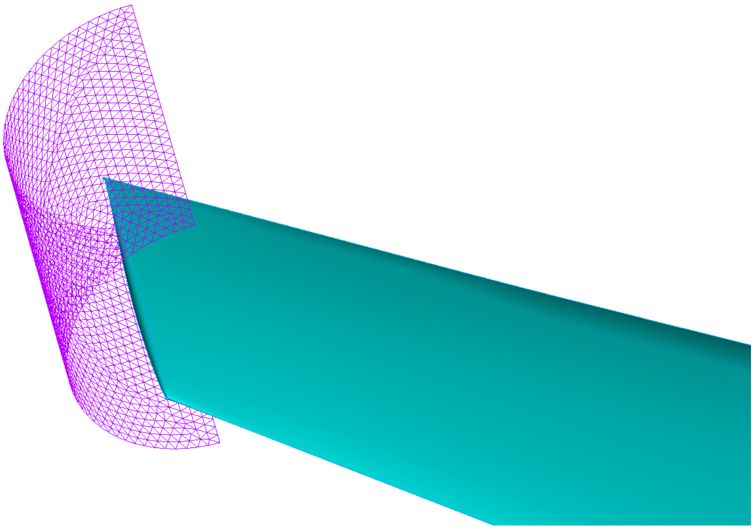

Figure 4.5 Baffle around the wing tip region

Chapter 5

Fluid-Surface Interface Library

Since a partitioned fully coupled approach was employed, there is the need to interface the fluid and structural modules and ensure conservation in doing so. The wing surface was defined in the fluid domain by hundreds of thousands of points to provide sufficient resolution of the flow field. In contrast, a hundred or so beam nodes are generally satisfactory to provide accurate resolution of the beam used to represent the wing structure. As mentioned previously, the forces on the skin nodes were passed to the beam nodes which were thereafter displaced by means of the structural code. Finally, the position of the wing is updated accordingly. Therefore, there is the need to ensure conservation of forces and moments when transferring the forces from wing surface to beam followed by the recovery of a smooth deformed wing surface.

5.1 Aerodynamic Force Interpolation

For the purpose of describing the theory used to develop the above functionality, consider a wing skin node with a force $\mathbf{f}_{aero}$ with components f_x, f_y and f_z acting in an arbitrary direction (Fig 5.1). If this skin node lies between two adjacent beam node planes (planes normal to each undeformed beam element node), then the aero forces are projected onto this beam element (the exception is the wing tip which is dealt with later). The height vector $\mathbf{h}$ is the vector of a projected point of the skin node onto the beam element such that $|\mathbf{h}|$ is a minimum. In the figure, a and b are the distances from node 0 and node 1 of

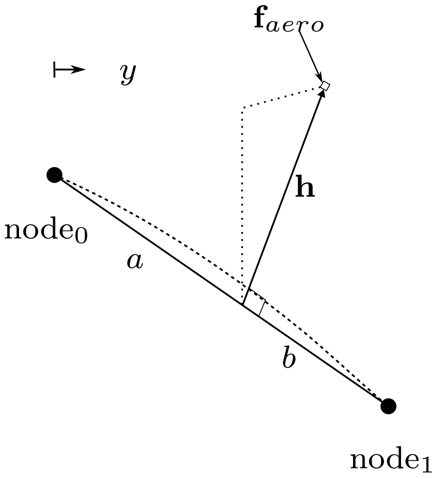

Figure 5.1 Schematic showing a force $\mathbf{f}_{aero}$ acting at a skin node and its relation to a beam element

the beam element to the projected point respectively and L is the length of the element. Force $\mathbf{f}_{aero}$ can be decomposed into components parallel and perpendicular to the beam element (due to the Euclidean framework employed). These decomposed components are then translated onto the projected point, with the addition of relevant moments.

Due to the discrete nature of the beam solver, the bending forces and moments are next distributed onto the beam nodes according to the methodology developed by McGuire and Gallagher [26] given in Figs 5.2 and 5.3. Torsion and forces parallel to the beam element are decomposed onto the beam nodes according to the ratio of the distance between the point of application and the beam nodes. This is illustrated for the torque in Fig 5.4.

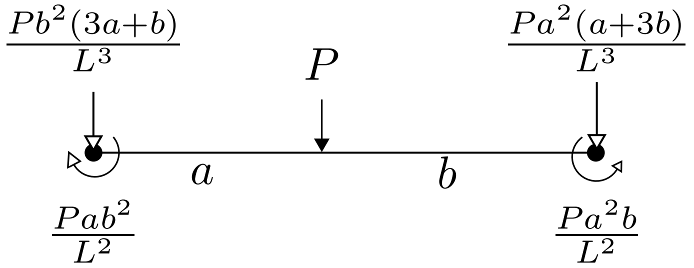

Figure 5.2 Diagram showing how a force P is projected onto the beam nodes. Adapted from McGuire et al.[26].

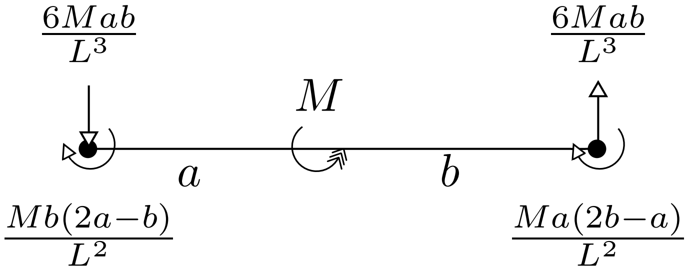

Figure 5.3 Diagram showing how a moment M is projected onto the beam nodes. Adapted from McGuire et al.[26].

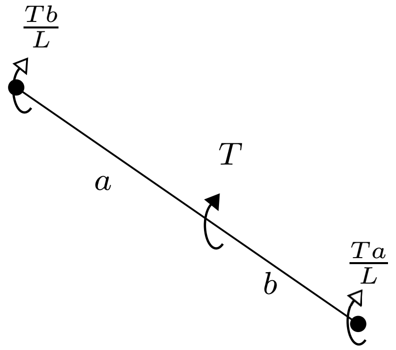

Figure 5.4 Schematic showing how a torque T acting on a beam element is distributed onto the beam nodes

These forces are then passed to the structural module that will compute the deformation of the beam and subsequently the new beam coordinates. From the new deformed beam position, the fluid mesh has to be updated accordingly. Using the parametric value $\frac{a}{L}$ and the vector $\mathbf{h}$, the skin node can be recreated from the beam node coordinates and therefore the skin node position recovered after deformation. However, as mentioned previously, the beam mesh resolution is generally orders less than the fluid mesh and a linear interpolation (between beam nodes) will result in a wing surface with discontinuous gradients. This would create unphysical distortions in the flow field.

The above wing skin crinkling was prevented by using a 3rd order interpolation via Bezier curves to approximate the beam element. This implies that the two curves from adjacent elements have the same tangent at the beam node they share so that the entire deformed beam may be interpreted as continuous with regards to deformation gradients.

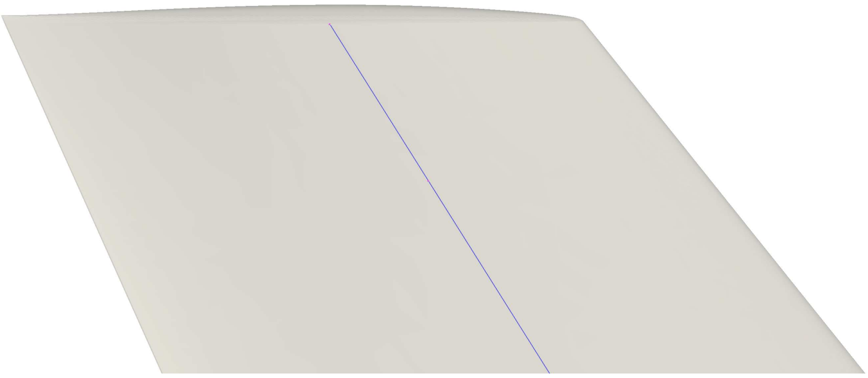

Figure 5.5 It can be seen that part of the wing tip extends past the end of the beam

Figure 5.6 Global coordinate system

The wing tip surface lies beyond the furthest beam element as shown in Fig 5.5. The above interpolation scheme therefore becomes problematic. To address this, the force is simply translated onto the last beam node with additional appropriate moments. As for the skin reconstruction, a fictitious rigid beam node was created by projecting linearly from the last beam element. The same method as used previously was then applied.

5.2 A Note on Coordinate System

As mentioned previously, the force $\mathbf{f}_{aero}$ is decomposed into components parallel and perpendicular to the beam element. This can be thought of as the force being rotated and translated from the CFD coordinate sytem to the beam local coordinate system. This creates the need to define the respective coordinate systems.

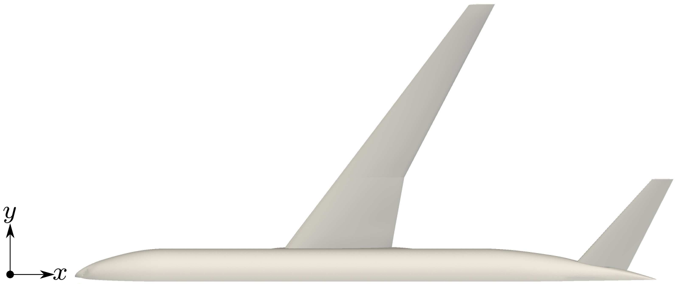

Figure 5.7 Global coordinate system employed for simulation purposes

The global coordinate system defines the aircraft in Cartesian coordinate in Euclieah space. By convention, the x-axis is in the streamwise direction and aligned with the fuselage of the aircraft, with positive pointing from the nose to the tail. The y-axis points (roughly) in the direction of the wing and the z-axis pointing vertically upwards. This is illustrated in Fig 5.6 and Fig 5.7. The origin is defined 2.35 m ahead of the nose [33]. The y-axis and the wing are not parallel as the aircraft has a swept back wing.

A local coordinate system with reference to the beam element was defined for the fluid. The local y-axis is parallel to the beam element with the positive y-axis pointing from node 0 to node 1. Note that each beam element has its own local reference frame and each element potentially has a different coordinate system. This coordinate system was used to decompose the forces as described in Section 5.1. The involved reference frame rotation and translation was effected by the shortest rotation from the global coordinate axes. Therefore this rotation is always less than 90 degrees.

5.3 Aerodynamic Force Application Procedure

As the beam solver requires forces in the global coordinate system, a multi-step transformation process is required. This commences by transforming $\mathbf{f}_{aero}$ to the beam local coordinate sytem by pre-multiplying with the transformation matrix, $\mathbf{T}^{GL}$ as shown in Eqn (5.1).

$$\mathbf{f}^{L}_{aero} = \mathbf{T}^{GL}\mathbf{f}^{G}_{aero} \tag{5.1}$$

The superscripts L and G denote the variable in local and global reference frame respectively. If $\mathbf{l}$ is the unit vector in the direction of the beam element with component l_x, l_y and l_z, the transformation matrix is given by:

$$\mathbf{T}^{GL} = \begin{pmatrix} l_z^2 + (1 - l_z^2)\cos\phi & -l_x \sin\phi & -l_x l_z\,(1 - \cos\phi) \\ l_x \sin\phi & \cos\phi & l_z \sin\phi \\ -l_x l_z(1 - \cos\phi) & -l_z \sin\phi & l_x^2 + (1 - l_x^2)\cos\phi \end{pmatrix} \tag{5.2}$$

where ϕ is the angle between the beam element and the global y-axis.

Next, the equivalent nodal loads can be calculated using the methodology described in Section 5.1 and the equations shown in Figures 5.2 to 5.4. These can be arranged in a matrix such that multiplying this matrix by the vector of local aero forces, $\mathbf{f}^{L}_{aero}$, will give the vector of forces acting on the beam nodes (Equation (5.3)) . This matrix was denoted by $\mathbf{R}_0$ for node 0.

$$\begin{pmatrix} f_x^L \\ f_y^L \\ f_z^L \\ M_x^L \\ M_y^L \\ M_z^L \end{pmatrix}_{struct_0} = \begin{pmatrix} \frac{b^2(3a+b)}{L^3} & 0 & 0 & 0 & 0 & \frac{6ab}{L^3} \\ 0 & \frac{b}{L} & 0 & 0 & 0 & 0 \\ 0 & 0 & \frac{b^2(3a+b)}{L^3} & -\frac{6ab}{L^3} & 0 & 0 \\ 0 & 0 & \frac{ab^2}{L^2} & -\frac{b(2a-b)}{L^2} & 0 & 0 \\ 0 & 0 & 0 & 0 & \frac{b}{L} & 0 \\ -\frac{ab^2}{L^2} & 0 & 0 & 0 & 0 & -\frac{b(2a-b)}{L^2} \end{pmatrix} \begin{pmatrix} f_x^L \\ f_y^L \\ f_z^L \\ -h_z^L f_y^L \\ h_z^L f_x^L - h_x^L f_z^L \\ h_x^L f_y^L \end{pmatrix}_{aero} \tag{5.3}$$

where the nomenclature is as previously defined.

However, the structural module requires the force in the global reference frame. Therefore, $\mathbf{f}^L_{struct}$ has to be pre-multiplied by the transformation matrix from the local to the global coordinate system, the latter being the inverse of matrix $\mathbf{T}^{GL}$.

$$\mathbf{f}^G_{struct} = \mathbf{T}^{LG}\mathbf{f}^L_{struct} \tag{5.4}$$

where the nomenclature is as previously defined.

Equation (5.1) and Equation (5.3) can be substituted into Equation (5.4) to give a more general expression for a specific node 0.

$$\mathbf{f}^G_{struct_0} = \left(\mathbf{T}^{LG}\mathbf{R}_0\mathbf{T}^{GL}\right)\mathbf{f}^G_{aero} \tag{5.5}$$

where the nomenclature is as previously defined.

The terms in brackets can be grouped into a force map matrix, $\mathbf{F}_M$. Since this force map only depends on the initial position of the skin nodes and the beam nodes, it does not change throughout the simulation. Therefore, it was constructed on initialisation, stored and then used throughout the simulation.

Chapter 6

Verification

To verify the correct use and accuracy of Elemental$^{®}$, various test cases were run. These are discussed next.

6.1 Beam Verification

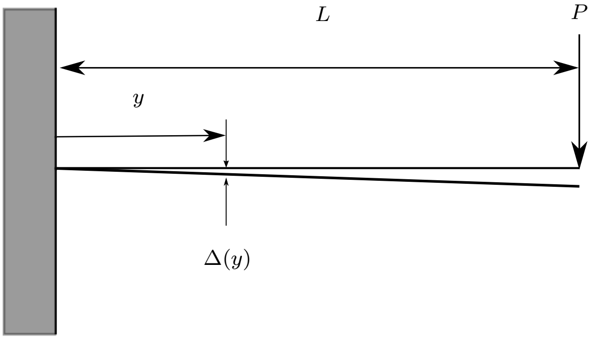

Figure 6.1 Schematic of analytical solution

To test the structural beam code, a simple test case was employed. A beam with 11 nodes, length 20 m and properties given in Table 6.1 was created. The beam was held fixed at one end (root) and a tip load of 10 kN was applied at the other end in a cantilever configuration. This test case was selected as it is similar to the loading of the wing in flight. Moreover an analytical solution is readily available and is given by Eq 6.1 [23].

Table 6.1 *Table of beam properties*

Properties	Symbol	Value
Length	L	20 m
Elastic modulus	E	200 GPa
Poisson ratio	ν	0.33
moment of Inertia	I	$3.89124 \times 10^{-05}\ m^4$
Second moment of Inertia	J	$7.7825 \times 10^{-05}\ m^4$
Shear strain correction factor	κ	0.833333

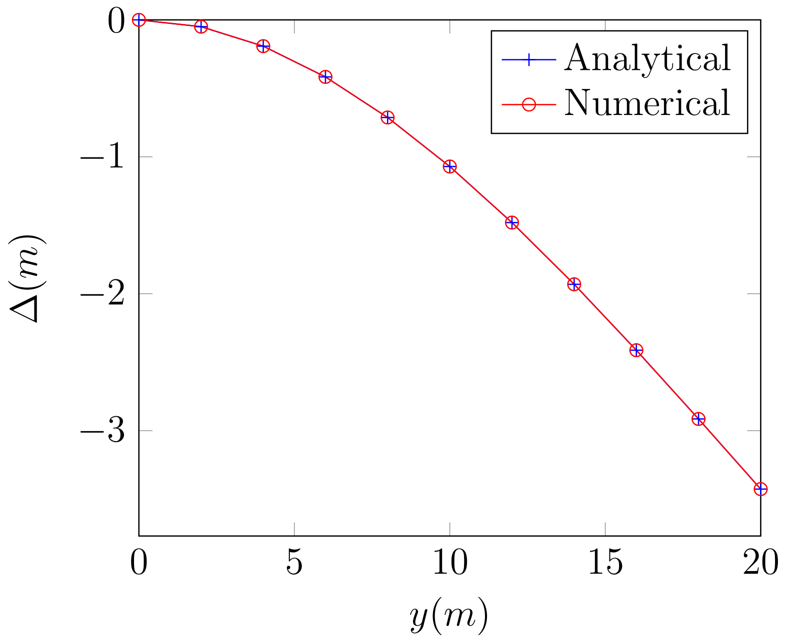

Figure 6.2 Graph of the numerical versus analytical deflection for a tip load

$$\Delta(y) = \frac{P\,(L-y)}{\kappa GA} + \frac{P\left(L^2\,(L-y) - \frac{(L-y)^3}{3}\right)}{2EI} - \frac{PL^3}{3EI} - \frac{PL}{\kappa GA} \tag{6.1}$$

where P is the tip load, A the area, Δ the deflection and y is the distance from the root. The other symbols are defined in Table 6.1.

The numerical solution was compared to the analytical solution and Fig 6.2 shows that an accurate solution was obtained.

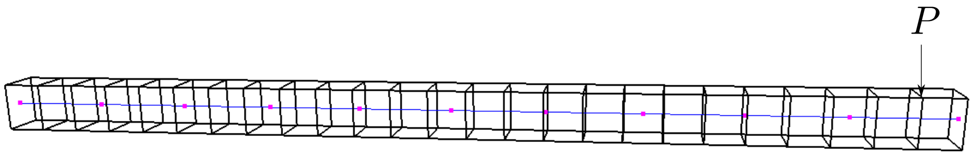

Figure 6.3 Schematic of the test beam. The structural mesh is displayed in blue and the edges of the skin mesh in black, with a node at each corner.

Ordinarily, a transient verificaiton would have to be performed at this stage. However, as mentioned before, the structural module was pre-existing in Elemental®. In a previous study, Farao [23] performed a dynamic verification by artificially applying an impulsive shear torsion at the free end of a cantilever beam . This was then compared to an analytical solution and it was found that the discrepancy was within 5%.

6.2 Interface Verification

To validate the developed interface, a cuboid of length 20 m, height and breadth 1 m was considered and a mesh with 26 x 2 x 2 nodes was created. This cuboid mimics the surface mesh of the wing and the same beam and configuration as in Section 6.1 was reused. A schematic is given in Figure 6.3 and a point force, P, of 10 kN was applied at (0.5, 19.2, 0.5). The force is translated onto the beam element and thereafter onto the beam nodes via application of the interface library. Subsequently, this causes both bending and twisting of the skin mesh. An analytical solution for a force acting on a Timoshenko cantilever beam at an arbitrary point is not readily available. Fortunately, the analytical solution for an Euler beam under aforementioned loading is available. Since the Timoshenko beam has already been validated in Section 6.1 and it is the interface that is under consideration here, the modelling code was reduced to an Euler-Bernoulli beam for the purpose of this test. The analytical deflection is given by Eqn 6.2 [43] and the twist τ by Eqn 6.3[44].

$$\Delta(y) = \begin{cases} \frac{Py^2}{6EI}(3a - y) & \text{for } 0 \leq y \leq a \\ \frac{Pa^2}{6EI}(3y - a) & \text{for } a \leq y \leq L \end{cases} \tag{6.2}$$

$$\tau(y) = \begin{cases} \frac{Ty}{GJ} & \text{for } 0 \leq y \leq a \\ \frac{Ta}{GJ} & \text{for } a \leq y \leq L \end{cases} \tag{6.3}$$

where a is the distance from the root to the point of application of force P, T is the torque, J is the polar moment of area and the other symbols are as previously defined.

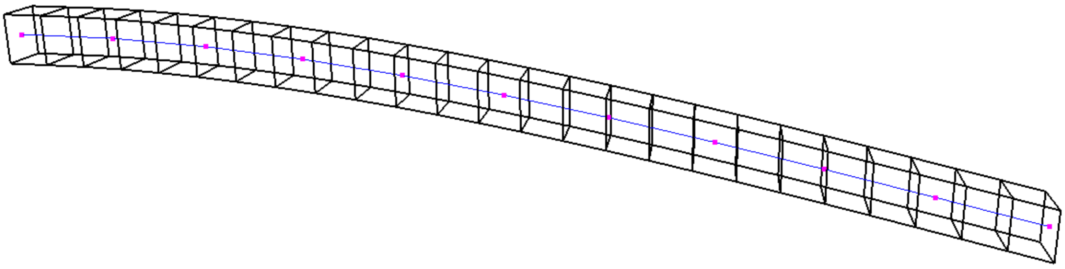

Figure 6.4 Test beam after it has been deformed

The numerical solution was compared to the analytical and Fig 6.5 and Fig 6.6 depict an exact correspondance. Moreover, the beam skin remains smooth and devoid of wrinkles. It is therefore concluded that the developed interface library is performing correctly.

A final test was conducted to evaluate the ability of the interface library to ensure wing skin smoothness on the actural CRM. This was done due to the complexity of the CRM geometry (containing a kink in sweep angle) while discontinuities would be both unphysical and affect the fluid solution adversely. An unusually large tip loading unlikely to occur under normal loading conditions was applied to the CRM wing. This caused a large deflection and the resulting deformed geometry was inspected. As shown in Fig 6.7 the resulting wing surface remained completely smooth.

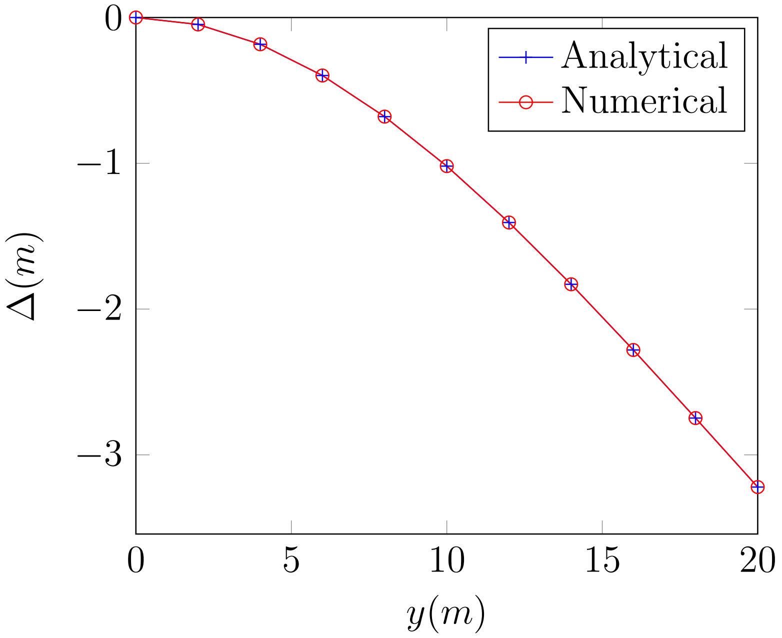

Figure 6.5 Graph of the numerical versus analytical deflection

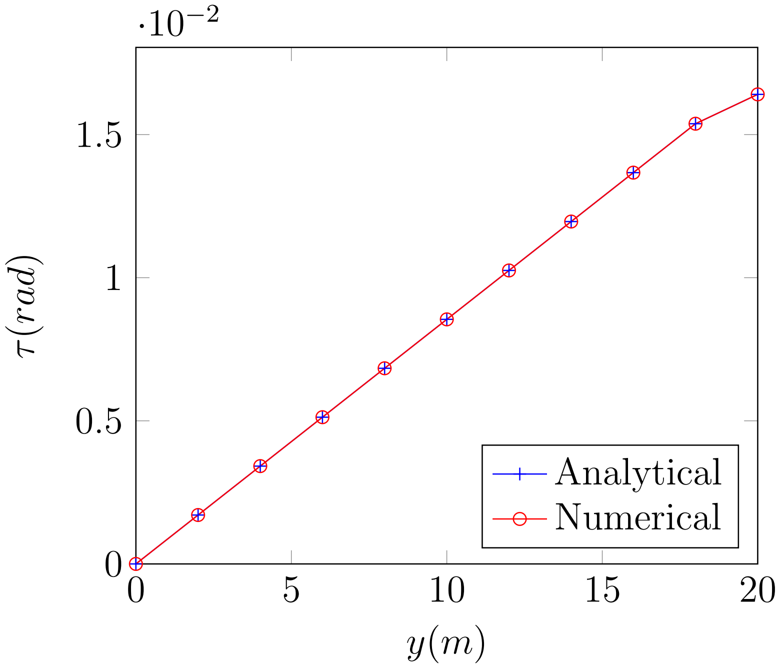

Figure 6.6 Graph of the numerical versus analytical twist

6.3 Fluid Verification

As the SBP-SAT boundary condition had not been used in an inviscid slip case before, a verification case was needed. To that effect, an inviscid steady transonic case was run on

Figure 6.7 Rear view of the CRM with the wing under extreme deformation

a 2D Naca 0012 aerofoil. The flow conditions employed were a Mach number of 0.8 and an Angle of Attack (AoA) of 1.25° at standard atmospheric conditions. An unstructured mesh with triangular cells and 4,988 nodes was used and the results were compared to those obtained from the Stanford University's code SU2 [45]. SU2 also used a triangular mesh with 5,233 points and the meshes can be seen in Fig 6.8. For the simulation, SU2 used a multigrid method with a Jameson-Schmidt Turkel (JST) scheme for spatial discretization.

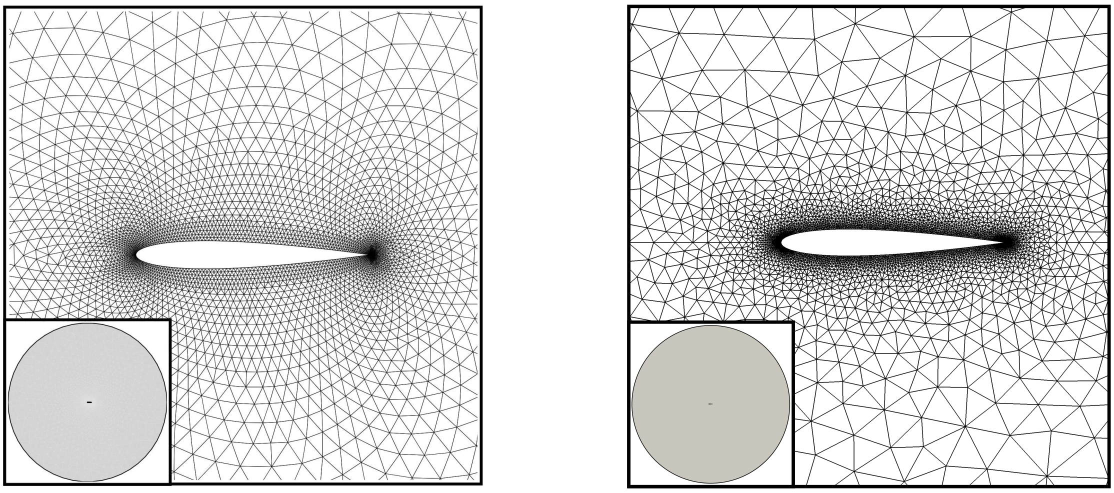

(a) Mesh used by SU2 for the Naca0012 **(b)** Mesh used in Elemental for the Naca0012

Figure 6.8 Meshes used for the steady Naca0012 verification

Fig 6.9 shows the pressure distribution around the airfoil in both SU2 and Elemental®. It can be seen that the pressure contours are comparable. Moreover, Fig 6.10 shows the C_p distribution on the airfoil surface for both simulations. Again, it can be seen that there is very good correlation, including in the vicinity of the shock.

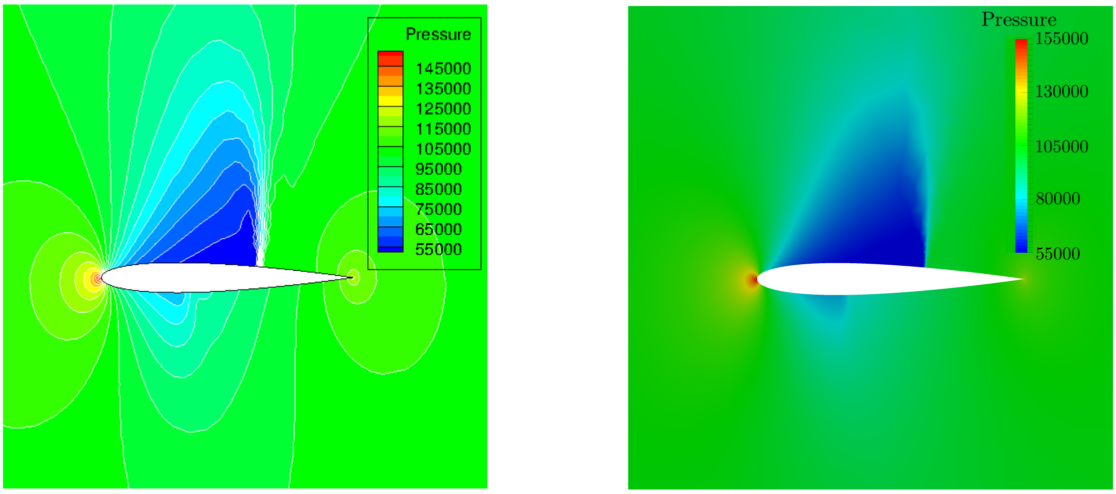

(a) Pressure distribution around the Naca 0012 in SU2

(b) Pressure distribution around the Naca 0012 in Elementa

Figure 6.9 Pressure distribution around the Naca 0012

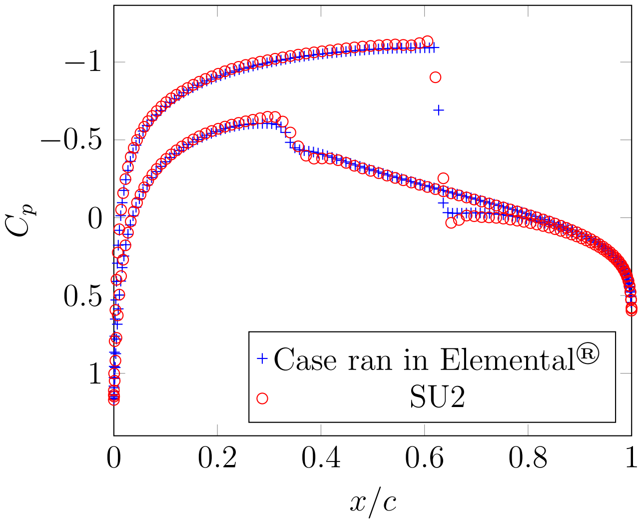

Figure 6.10 Comparison of the C_p values on the airfoil surface on the Naca 0012

6.4 Mesh Resolution and Mesh Independence

A mesh refinement study is routine for CFD calculations to ensure that a solution independent of the mesh resolution is obtained. In his work on vortex propagation, Changfoot performed a mesh independence study on the CRM geometry where steady state calculations in Elemental® for a Mach number of 0.85 and AoA 0° was performed [39]. He then concluded that the coarse, medium and fine mesh was in the asymptotic region. Following a Grid Convergence Index (GCI) comparison on the overall lift coefficient, Changfoot then used the coarse mesh to obtain a reasonable trade off between accuracy and computational cost.

This works differs from the one by Changfoot in that the actual lift distribution over the length of the wing is important. This warrants considering pressure distributions across various wing spans. It was therefore endeavoured to assess mesh sensitivity to this while generating a mesh of cost midway between the coarse and medium meshes of the aforementioned author. Changfoot's coarse mesh was used as a starting point and a blend of the coarse and medium meshes produced. The computed pressure distribution is depicted in Fig 6.11. Steady inviscid simulations were then run at Ma = 0.86 on the coarse and the refined mesh and the C_p plots at different span-wise locations along the wing were compared. Fig 6.12 shows that there is very good correlation between the two meshes.

Convergence was deemed to be achieved when the residual had dropped by 5 orders. In addition, the value of interest (in this case the C_L) was monitored to determine whether it had reached a constant value at the end of the simulation.

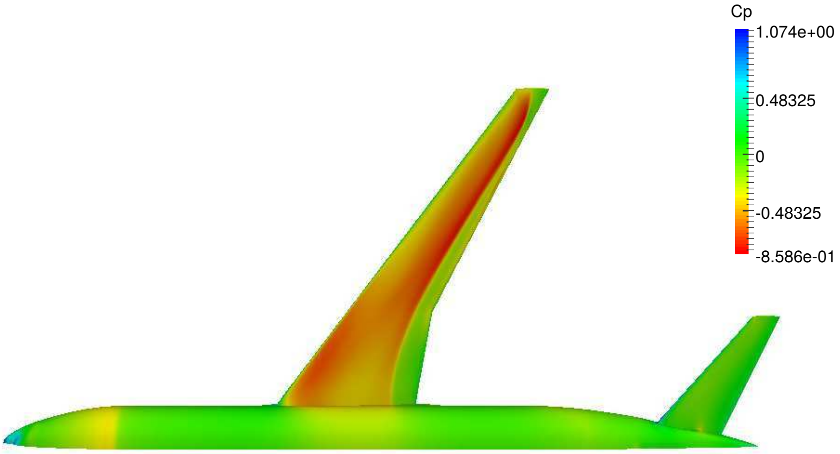

Figure 6.11 C_p distribution on the CRM at Ma = 0.86 and AoA = 0 deg

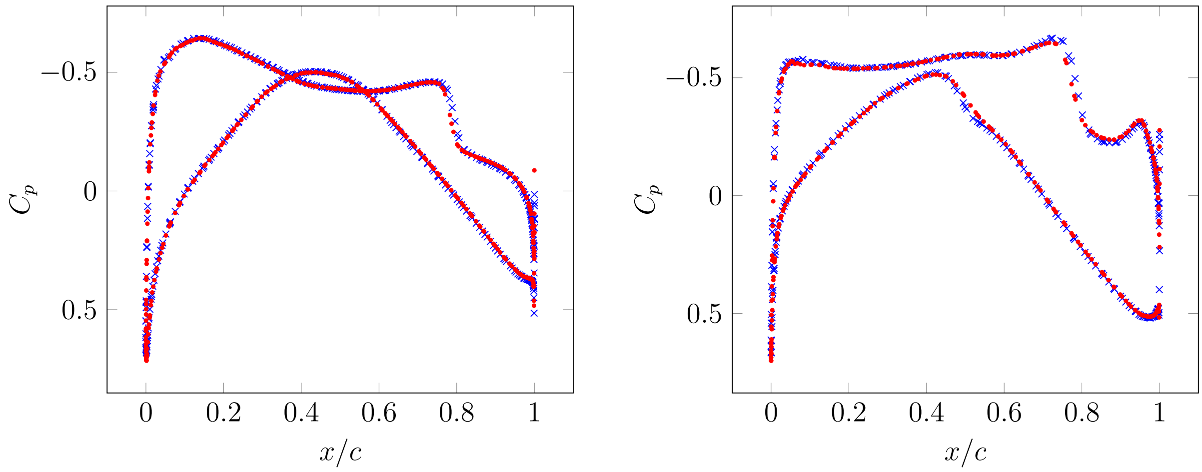

(a) 16.4 % Span **(b)** 38.6 % Span

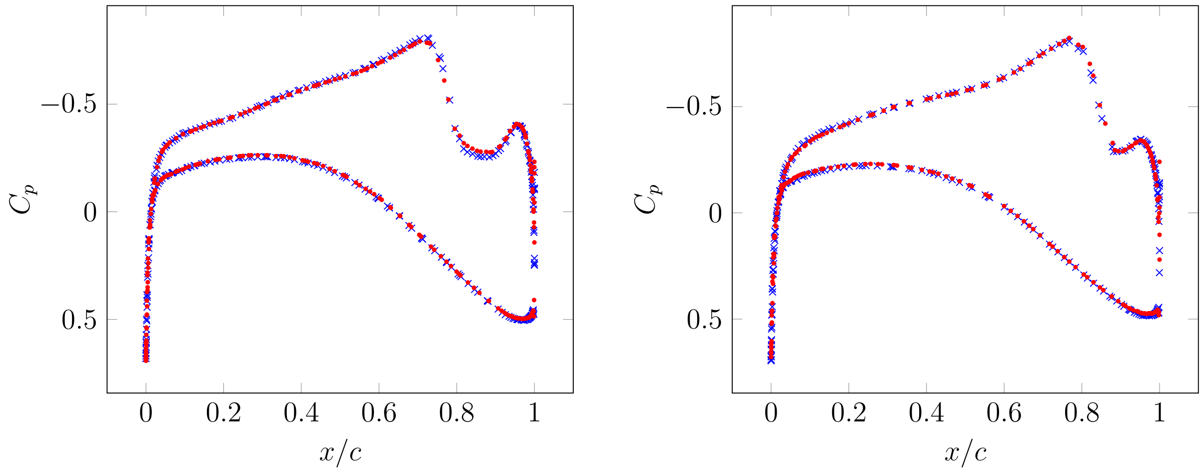

(c) 60.9 % Span **(d)** 83.3 % Span

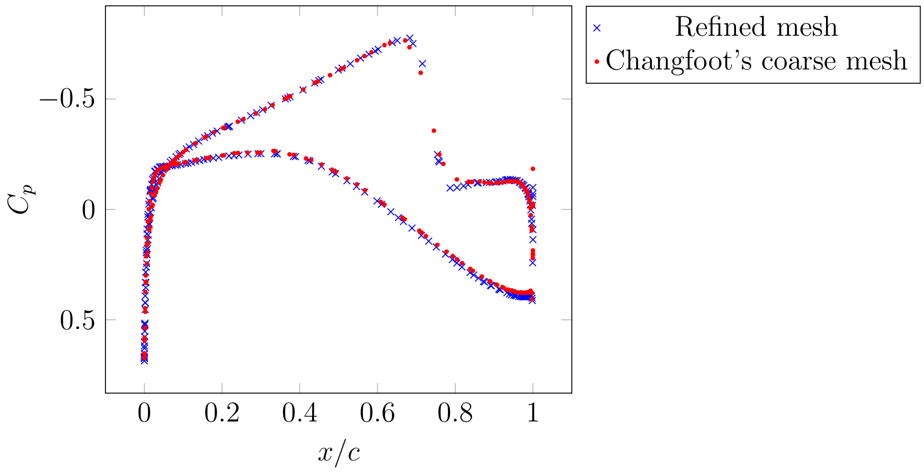

(e) 94.4 % Span

Figure 6.12 Graphs of the C_p values as a function of the local normalised chord length at different spans for Ma = 0.86

Chapter 7

Results

A simulation was performed on a transonic CRM geometry under gust loads. A steady state calculation was performed until convergence before the transient effects of the gust were introduced into the domain. The mesh and interface library as outlined previously were employed for this purpose. Due to time constraints on the project, the fully coupled FSI was not conducted. Instead, a simulation was performed first on a rigid aircraft and the force history on the wing recorded. This was then applied to the beam code to compute the aeroelastic response. The results were then compared with the fully coupled calculations of Wales et al. [46].

Fig 7.1 shows that there is good correlation between the two results, where the peak tip displacement and the period are accurately predicted even if present work under-predicts the negative peak amplitude compared to Wales et al. The disparity in maximum tip displacement is 8 %. Furthermore, Wales el al.'s displacement was smaller due to the wing accelerating upwards which reduced the effective gust velocity.

Fig 7.2 shows the C_p distribution over the aircraft at time t = 0.2. The same scale as Fig 6.11 was used and it can be seen that the shock is more pronounced in the gust case. Finally the Cp distributions with and without gust peak are shown compared in Fig 7.3.

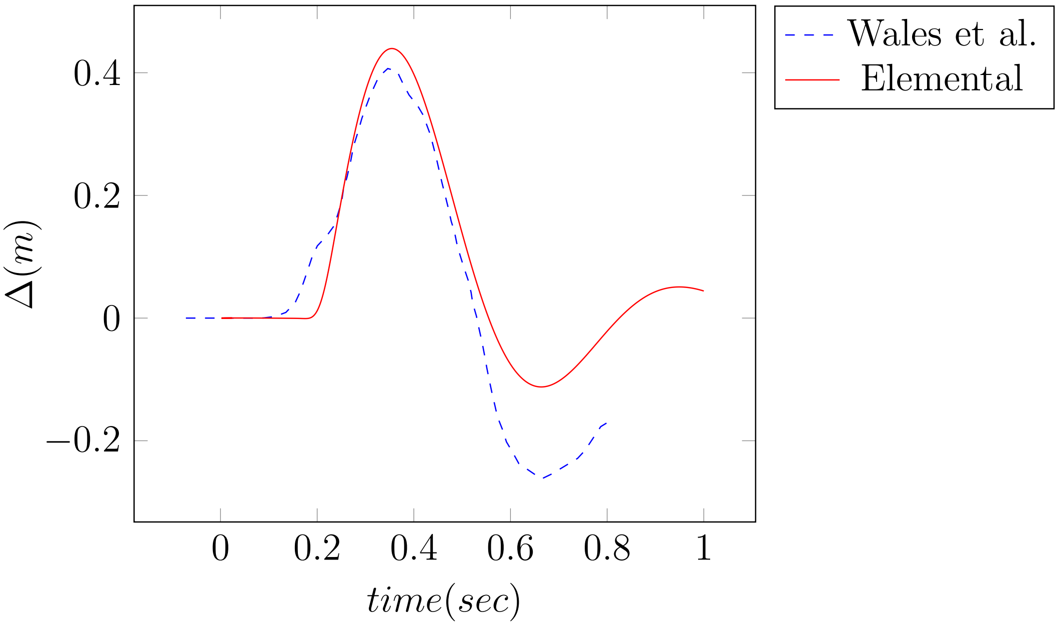

Figure 7.1 Comparison of the tip displacement obtained from Elemental® rigid and Wales flexible wing

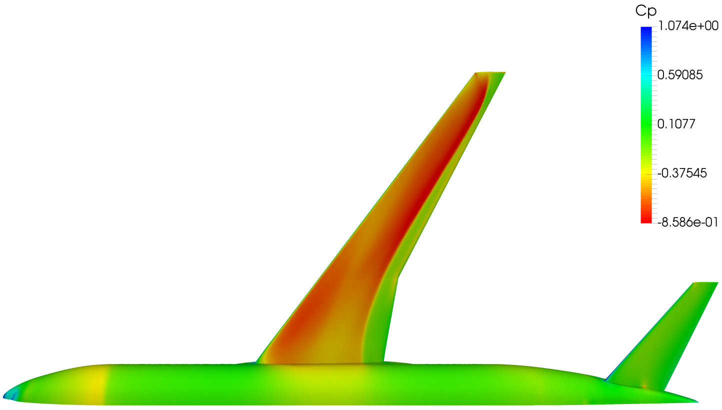

Figure 7.2 C_p distribution on the CRM at time t = 0.2

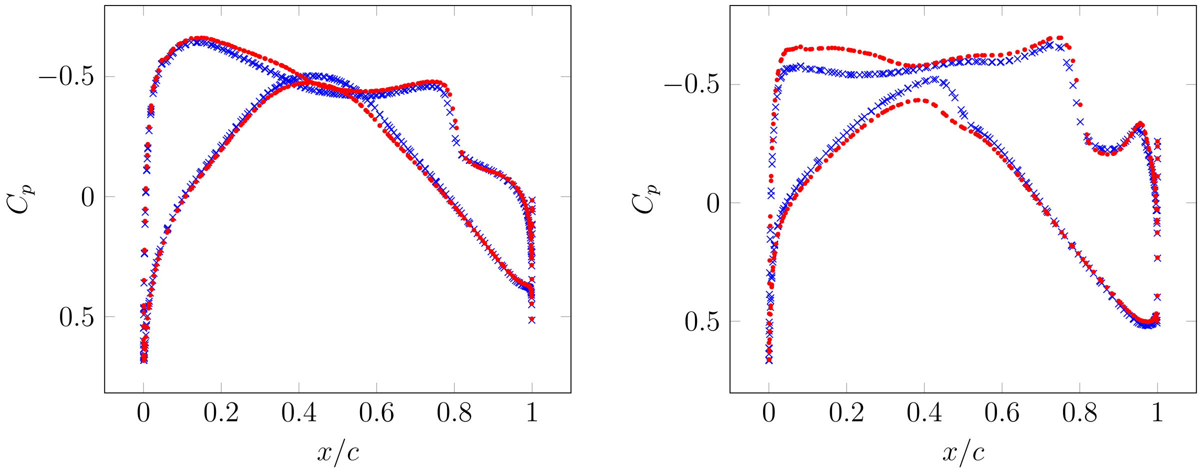

(a) 16.4 % span **(b)** 38.6 % span

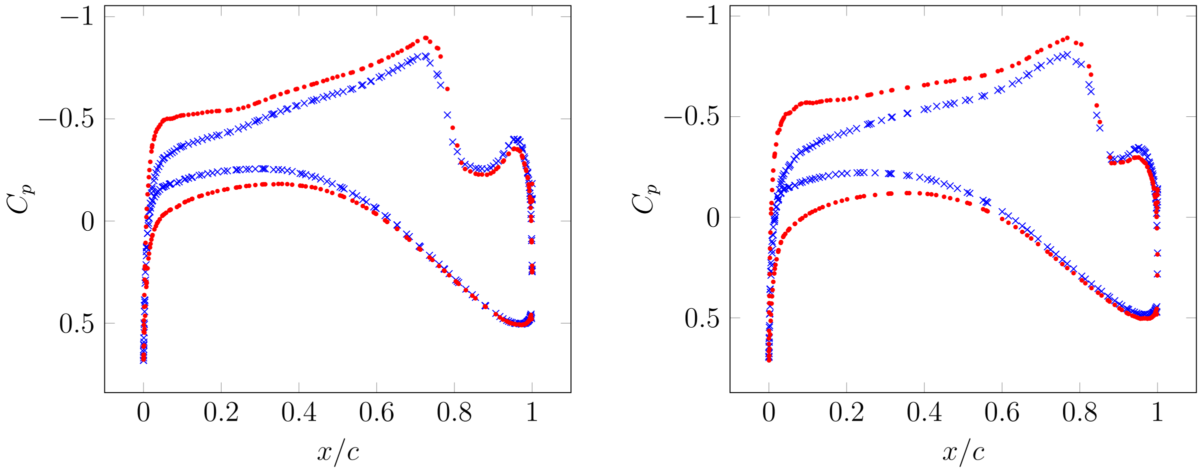

(c) 60.9 % span **(d)** 83.3 % span

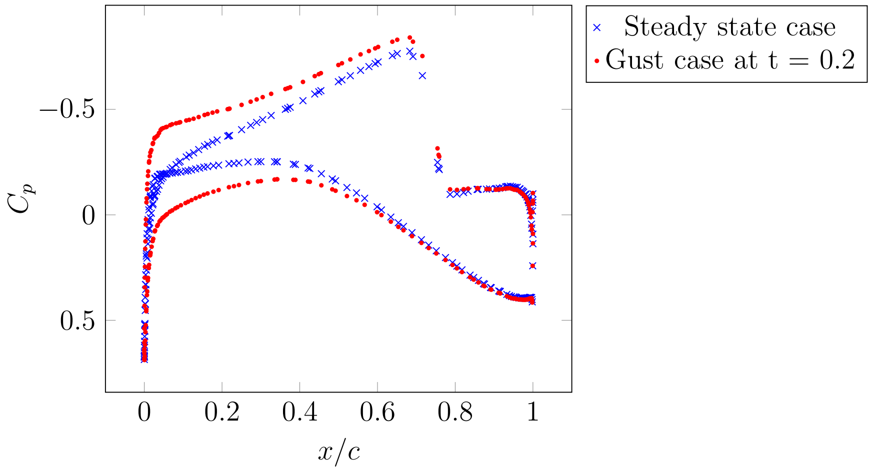

(e) 94.4 % span

Figure 7.3 C_p values as a function of the local normalised chord length at different spans.

Chapter 8

Discussion, Conclusion and Recommendation

The aim of this project was to develop a framework to perform aeroelastic simulation on a whole aircraft model under gust loading. This required the combined use of various aspects of the Elemental® software viz. 3D beam modelling code as well as compressible flow module. The latter was extended to account for propagating gusts, while the joint use of features was facilitated via the development of a beam-wing interface library. Different aspects of the framework were individually assessed and tested. It was found that each individual component performed as expected and the accuracy of the interface library was verified using analytical test cases. Moreover, the robustness of the surface mesh deformation and displacement projection was also demonstrated by artificially deforming the wing and successfully recovering a smooth surface even for very large deformations.

An $18.288m$ long gust was applied to a rigid CRM aircraft at $\mathrm{Ma} = 0.86$ and the aerodynamic forces on the wing were used to calculate a pseudo wing deflection. The result was compared with the work of Wales et al. and the tip displacement obtained was similar with the peak amplitude differing by only 8 %. The small error in tip displacement demonstrates that the framework is viable even if further investigation is required before asserting the validity of the framework with confidence.

8.1 Recommendation for Future Work

First and foremost, a fully coupled FSI calculation is to be performed by completing the 3D mesh movement algorithm in Elemental®. Next, the Aerogust consortium recommends three different gust length, 30, 150 and 350 ft. Due to the cost of computation, only the shortest gust was investigated. However, performing further simulations on all recommended gust lengths would give more data points to compare and give confidence in the framework. A larger gust length would also result in a bigger tip displacement and as the deflections become larger, the linear regime might be exceeded. Therefore, a non-linear structural model should be implemented. This would enable a more accurate prediction of the deflection as well as assessing the degree of non-linearity generated and the necessity to model such non-linearities. In turn, this would enable the investigation and suitability of highly flexible materials for the wing composition.

References

[1] M. Darecki, C. Edelstenne, T. Enders, E. Fernandez, P. Hartman, J.-P. Herteman, M. Kerkloh, I. King, P. Ky, M. Mathieu *et al.*, “Flightpath 2050 europes vision for aviation,” *Off. Eur*, 2011.

[2] European Commission, “Horizon 2020 work programme 2016 - 2017 11 . smart , green and integrated transport,” no. July 2016, 2016.

[3] W. D. Nordhaus, “The progress of computing,” 2001, Yales Cowles Foundation discussion paper No. 1324.

[4] A. Jameson, “Time dependent calculations using multigrid, with applications to unsteady flows past airfoils and wings,” in *10th Computational Fluid Dynamics Conference*, 1991, p. 1596.

[5] M.-H. Lallemand, H. Steve, and A. Dervieux, “Unstructured multigridding by volume agglomeration: Current status,” *Computers and Fluids*, vol. 21, no. 3, pp. 397 – 433, 1992.

[6] J. C. Vassberg, E. N. Tinoco, M. Mani, B. Rider, T. Zickuhr, D. W. Levy, O. P. Brodersen, B. Eisfeld, S. Crippa, R. A. Wahls *et al.*, “Summary of the fourth AIAA computational fluid dynamics drag prediction workshop,” *Journal of Aircraft*, 2014.

[7] A. Sclafani, M. DeHaan, J. Vassberg, C. Rumsey, and T. Pulliam, “Drag prediction for the NASA CRM wing-body-tail using cfl3d and overflow on an overset mesh,” in *28th AIAA Applied Aerodynamics Conference*, 2010, p. 4219.

[8] S. Keye and R. Rudnik, "Validation of wing deformation simulations for the NASA CRM model using fluid-structure interaction computations," in *53rd AIAA Aerospace Sciences Meeting*, 2015, p. 0619.

[9] I. Garrick and W. H. Reed III, "Historical development of aircraft flutter," *Journal of Aircraft*, vol. 18, no. 11, pp. 897–912, 1981.

[10] Aerogust consortium, "Aeroelastic gust modelling (Aerogust)," Aug. 2014, Aerogust Proposal Document.

[11] E. Albano and W. P. Rodden, "A doublet-lattice method for calculating lift distributions on oscillating surfaces in subsonic flows." *AIAA journal*, vol. 7, no. 2, pp. 279–285, 1969.

[12] J. Murua, R. Palacios, and J. M. R. Graham, "Applications of the unsteady vortex-lattice method in aircraft aeroelasticity and flight dynamics," *Progress in Aerospace Sciences*, vol. 55, pp. 46–72, 2012.

[13] L. Reimer, M. Ritter, R. Heinrich, and W. Krüger, "Cfd-based gust load analysis for a free-flying flexible passenger aircraft in comparison to a dlm-based approach," in *22nd AIAA Computational Fluid Dynamics Conference*, 2015, p. 2455.

[14] J. Donea, J.-P. Ponthot, and A. Rodriguez Ferran, *Encyclopedia of Computational Mechanics.* Chichester: John Wiley, 2004, ch. 14.

[15] A. G. B. Mowat, "Modelling of non-linear aeroelastic systems using a strongly coupled fluid-structure-interaction methodology," Master's thesis, University of Pretoria, 2012.

[16] R. Suliman, O. F. Oxtoby, A. Malan, and S. Kok, "A matrix free, partitioned solution of fluid–structure interaction problems using finite volume and finite element methods," *European Journal of Mechanics-B/Fluids*, vol. 49, pp. 272–286, 2015.

[17] M. Souli, A. Ouahsine, and L. Lewin, "ALE formulation for fluid–structure interaction problems," *Computer methods in applied mechanics and engineering*, vol. 190, no. 5-7, pp. 659–675, 2000.

[18] C. Wales, D. Jones, and A. Gaitonde, "Prescribed velocity method for simulation of aerofoil gust responses," *Journal of Aircraft*, vol. 52, no. 1, 2015.

[19] D. E. Raveh, "CFD-based gust response analysis of free elastic aircraft," *ASD Journal*, vol. 2, no. 1, pp. 23–34, 2010.

[20] D. E. Raveh, "Gust-response analysis of free elastic aircraft in the transonic flight regime," *Journal of Aircraft*, vol. 48, no. 4, pp. 1204–1211, 2011.

[21] P. Bekemeyer, R. Thormann, and S. Timme, "Rapid gust response simulation of large civil aircraft using computational fluid dynamics," *The Aeronautical Journal*, vol. 121, no. 1246, pp. 1795–1807, 2017.

[22] C. Valente, C. Wales, A. Gaitonde, J. Cooper, and Y. Lemmens, "An optimized doublet-lattice method correction approach for a large civil aircraft," in *Proceedings of the 17th International Forum on Aeroelasticity and Structural Dynamics*, 2015, pp. 591–606.

[23] J. C. Farao, "Toward a full aircraft model platform for fuel slosh-structure interaction simulations," Master's thesis, University of Cape Town, 2015.

[24] C. Valente, D. Jones, A. Gaitonde, J. Cooper, and Y. Lemmens, "OpenFSI interface for strongly coupled steady and unsteady aeroelasticity." in *Proceedings of the 17th International Forum on Aeroelasticity and Structural Dynamics*, 2015, pp. 591–606.

[25] C. Kaiser, D. Friedewald, and J. Nitzsche, "Comparison of nonlinear CFD with time-linearized CFD and CFD-corrected DLM for gust encounter simulations," in *Proceedings of the 17th International Forum on Aeroelasticity and Structural Dynamics*, 2017.

[26] W. McGuire and R. H. Gallagher, *Matrix structural analysis*, 2nd ed. Wiley, 2000.

[27] J. R. Shewchuk, "Triangle: Engineering a 2D quality mesh generator and Delaunay triangulator," in *Applied computational geometry towards geometric engineering.* Springer, 1996, pp. 203–222.

[28] J. Vassberg, M. Dehaan, M. Rivers, and R. Wahls, "Development of a common research model for applied CFD validation studies," in *26th AIAA Applied Aerodynamics Conference*, 2008, p. 6919.

[29] "NASA Common Research Model," https://commonresearchmodel.larc.nasa.gov/, accessed: 2017-11-30.

[30] C. Wales, C. R. G., A. Gaitonde, and D. Jones, "Comparison of aerodynamic models for 1-cosine gust loads prediction," in *Proceedings of the 17th International Forum on Aeroelasticity and Structural Dynamics*, 2017.

[31] R. Cook and C. Wales, "Aeroelastic gust modelling, 12 month meeting, University of Bristol," Presentation, 2016.

[32] J. R. Wright and J. E. Cooper, *Introduction to aircraft aeroelasticity and loads.* John Wiley & Sons, 2008, vol. 20.

[33] T. Klimmek, "Parametric set-up of a structural model for fermat configuration aeroelastic and loads analysis," *Journal of Aeroelasticity and Structural Dynamics*, vol. 3, no. 2, 2014.

[34] M. Iatrou, C. Wales, K. Renouil, A. Gaitonde, and D. Jones, "D5.6 report reviewing test cases and identifying any modifications as a result of 1 year work," Airbus, UoB, Valeol, Tech. Rep., 2016.

[35] A. Jameson, W. Schmidt, E. Turkel *et al.*, "Numerical solutions of the Euler equations by finite volume methods using Runge-Kutta time-stepping schemes," *AIAA paper*, vol. 1259, p. 1981, 1981.

[36] Y. Zhao and A. Forhad, "A general method for simulation of fluid flows with moving and compliant boundaries on unstructured grids," *Computer Methods in Applied Mechanics and Engineering*, vol. 192, no. 39–40, pp. 4439–4466, 2003.

[37] E. Toro, *Riemann solvers and numerical methods for fluid dynamics.* Springer-Verlag, 2009.

[38] J. Blazek, *Computational fluid dynamics: principles and applications*, 2nd ed. Elsevier, 2001.

[39] D. Changfoot, "Towards a hybrid CFD platform for investigating aircraft trailing vortices," Master's thesis, University of Cape Town, 2017.

[40] J. Fish and T. Belytschko, *A first course in finite elements.* John Wiley & Sons Limited, 2007.

[41] L. Andersen and S. R. Nielsen, "Elastic beams in three dimensions," 2008.

[42] H. P. Gavin, "Numerical integration in structural dynamics," Fall 2016.

[43] R. C. Juvinall and K. M. Marshek, *Machine component design.* Wiley, 2013.

[44] E. J. Hearn, *Mechanics of Materials Volume 1: An Introduction to the Mechanics of Elastic and Plastic Deformation of Solids and Structural Materials: v. 1.* Butterworth-Heinemann, 1997.

[45] "Su2 quick start," https://github.com/su2code/SU2/wiki/Quick-Start, accessed: 2017-01-24.

[46] C. Wales, A. Gaitonde, and D. Jones, "D2.3 report on the prediction of nonlinear beheavious using field and split velocity methods," University of Bristol, Tech. Rep., 2016.